Flight dynamics in *Drosophila* through a dynamically-scaled robotic approach

Thesis by

Michael J. Elzinga

In Partial Fulfillment of the Requirements

for the Degree of

Doctor of Philosophy

California Institute of Technology

Pasadena, California

2013

(Defended December 14, 2012)

To Carter and Connor.

Acknowledgments

I owe a debt of gratitude to all of the people in my life that provided support, encouragement and their expertise to make the completion of this project possible. A heartfelt thank you goes to my advisor, Michael Dickinson. And, if it were up to Michael, that is where his recognition would end, with a brief, but polite, nod to his role in this whole endeavor. This in and of itself speaks to one of the many reasons I have such admiration for him both as a scientist and as a person. Since this is the one section of this dissertation that will escape the wrath of his editor's pen, I think I'll elaborate. I happily credit Michael for the enjoyable and intellectually satisfying graduate experience that I've had over these many years. His mentorship and example have made an indelible impact on my life. His input and expertise are present in all of the work presented here. I should also mention that Michael's constructive comments on my last manuscript inspired the theme of the quotes throughout this thesis. I leave it as an exercise to the reader to guess the theme, and for those who know Michael, to speculate on the nature of these comments.

I would like to thank the members of my committee, Kaushik Bhattacharya, Richard Murray, and Joel Burdick for the time that they have put into providing thoughtful feedback. Both Kaushik and Richard have provided much-appreciated guidance and discussions from my first semester at Caltech until now.

I want to thank the entire Dickinson lab, both current members and alumni, but especially Wyatt Korff, who gave me my initiation into the lab and was a great mentor and friend throughout. I also have a strong suspicion that Wyatt had a hand in convincing Michael that I was worth keeping around during my early months in the lab. William Dickson taught me everything I know about programming, either directly, or

indirectly through the incredibly well written projects that he made accessible. The software and mechatronics development work that both Will and Peter Polidoro performed made much of this dissertation possible. Will was also a collaborator on the manuscript that formed the basis for Chapter 2, and many of the experiments were designed and carried out together. Floris van Breugel, my officemate after the move to Seattle, was the source of many stimulating discussions. He was also a co-author on much of the material in Chapter 3, to which he made conceptual contributions. I engaged in many enjoyable discussions around the coffee pot with Francisco Zabala, Florian Muijres, and numerous other Dickinson lab members that both my work and my life benefited from greatly. If there is anyone who embodies the Dickinson lab culture, it is Peter Weir. He represents what made the work environment both productive and enjoyable.

Vedran Coralic, Madeline Miller, and others that I entered the ME program with were not only allies in the battle against coursework and qualifying exams, but good friends as well. Jon Farrar, a close friend and one of my college roommates, was perhaps my only friend outside of academia who read my first manuscript and provided insightful comments. Paul Hanson has been there for me since I was 8 years old and continues to provide encouragement to both me and my family.

My parents, brother, and grandparents have provided an endless supply of encouragement and models of hard work and good values. My wife, Bonnie, and my two boys, Carter and Connor, are a constant reminder of what is truly important in life. Their love and support knows no bounds. I also want to thank the boys for feigning excitement at bedtime stories based on earlier drafts of this thesis.

Flies are nature's fighter jets.

—Unknown[1]

---

[1] This quote is often attributed to Michael Dickinson although he is not quite sure how such credit originated.

Abstract

Flies are particularly adept at balancing the competing demands of delay tolerance, performance, and robustness during flight, which invites thoughtful examination of their multimodal feedback architecture. This dissertation examines stabilization requirements for inner-loop feedback strategies in the flapping flight of *Drosophila*, the fruit fly, against the backdrop of sensorimotor transformations present in the animal. Flies have evolved multiple specializations to reduce sensorimotor latency, but sensory delay during flight is still significant on the timescale of body dynamics. I explored the effect of sensor delay on flight stability and performance for yaw turns using a dynamically-scaled robot equipped with a real-time feedback system that performed active turns in response to measured yaw torque. The results show a fundamental tradeoff between sensor delay and permissible feedback gain, and suggest that fast mechanosensory feedback provides a source of active damping that compliments that contributed by passive effects. Presented in the context of these findings, a control architecture whereby a haltere-mediated inner-loop proportional controller provides damping for slower visually-mediated feedback is consistent with tethered-flight measurements, free-flight observations, and engineering design principles.

Additionally, I investigated how flies adjust stroke features to regulate and stabilize level forward flight. The results suggest that few changes to hovering kinematics are actually required to meet steady-state lift and thrust requirements at different flight speeds, and the primary driver of equilibrium velocity is the aerodynamic pitch moment. This finding is consistent with prior hypotheses and observations regarding the relationship between body pitch and flight speed in fruit flies. The results also show that the dynamics may be stabilized with additional pitch damping, but the

magnitude of required damping increases with flight speed. I posit that differences in stroke deviation between the upstroke and downstroke might play a critical role in this stabilization. Fast mechanosensory feedback of the pitch rate could enable active damping, which would inherently exhibit gain scheduling with flight speed if pitch torque is regulated by adjusting stroke deviation. Such a control scheme would provide an elegant solution for flight stabilization across a wide range of flight speeds.

Contents

List of Figures

List of Tables

Chapter 1

Introduction

Just as the Wright brothers implemented controls to achieve stable airplane flight, flying insects have evolved behavioral strategies that ensure recovery from flight disturbances.

—Leif Ristroph (2010)

The variety and complexity of aerial maneuvers of insects have fascinated biologists and aerospace engineers, leading to a concerted effort to understand the aerodynamics of flapping flight as well as how the requisite forces and moments are generated and controlled. Although the use of dynamically scaled robots and computational fluid dynamics have led to an understanding of the unsteady mechanisms that explain the elevated gross force production required for achieving sufficient lift (Ellington et al., 1996; Dickinson et al., 1999; Sane, 2003; Maxworthy, 1981), the relationship among sensory information processing, wing kinematic changes and aerodynamic force modulations required for performing maneuvers and maintaining stable flight remains an active area of research (Dickinson, 2006; Sugiura and Dickinson, 2009; Wang et al., 2008). The neuromuscular architecture of a fly's wing hinge is quite complicated, and it enables the animal to generate a large range of different stroke patterns during flight to meet these control demands (Balint and Dickinson, 2004; Wisser and Nachtigall, 1984). However, despite the large kinematic space a fly might use and the nonlinear nature of their flight dynamics, studies suggest that flies utilize surprisingly simple and elegant flight control solutions.

The advantages of a simplified flight control scheme are evident when considering the temporal cost of increasingly complex computations and the performance constraints imposed by neural delays (Cowan et al., 2006; Elzinga et al., 2012). Feedback delays can induce fundamental performance limits or even destabilize an otherwise stable system (Aström and Murray, 2010). Neural processing delays may, therefore, have a profound impact on the dynamics and control of biological systems. For example, delay plays a crucial role in dictating constraints on the architecture of a stabilizing controller in cockroach wall following behavior (Cowan et al., 2006). For the fly, neural processing delays are substantial relative to the fast time scale of their flight dynamics (Taylor and Krapp, 2008; Fry et al., 2003). Researchers have highlighted the importance of passive stabilizing mechanisms in flapping flight (Hesselberg and Lehmann, 2007; Hedrick et al., 2009) which would not be subject to processing delays, but active, sensory-based equilibrium reflexes in flies are still prevalent and compulsory for the robust flight behavior for which flies are so well known (Parsons et al., 2010; Taylor and Krapp, 2008; Dickinson, 1999; Sherman and Dickinson, 2003). The ability of flies and other insects to navigate and fly stably in the presence of significant feedback delays motivates an in-depth look at the influence these delays have on system dynamics.

1.1 Sensorimotor transformations in flight

Flies are endowed with a multitude of sensors to richly sample their environment and allow for feedback during locomotion (Taylor and Krapp, 2008). Readily apparent and perhaps the least understood in terms of their role in flight control is the large number of innervated hairs on the wings and elsewhere on the body which could serve as airflow sensors (Burrows, 1996). The wings also possess numerous campaniform sensilla that may provide a measure of wing loading and have been shown to elicit compensatory head movements (Hengstenberg, 1988). The antennae itself performs a diverse number of functions including chemosensation, mechanosensation, thermosensation, and, possibly most relevant to the discussion of flight stabilization, airspeed

detection (Burkhardt and Gewecke, 1965; Hollick, 1940; Fuller, 2011). Further, flies can actively position their antennae, leading to a sensor that is highly adaptive. An auxiliary visual system of three single lens ocelli forms an under-focused image and due to the large axonal diameter and wide receptive of ocellar interneurons in addition to their triangular arrangement could act as a fast horizon detector (Krapp, 2009). This dissertation will restrict its focus to a subset of the sensory systems available to the fly which are widely studied, essential to flight control, and that reside on opposite ends of the sensorimotor delay spectrum: the visual system and the halteres. The halteres serve a number of functions and will be discussed in more detail, but, for for the sake of the current discussion, they can be considered to function as vibrating gyroscopes that provide a measure of rotation rate (Pringle, 1948; Nalbach and Hengstenberg, 1994). A likely corollary to the disparity in sensorimotor delay between the two systems is in the richness of information collected, due to the computation time required for the reduction of information to behaviorally relevant quantities. In this sense, the sensorimotor delays associated with the halteres and with the visual system provide bounds on the important timescales and a contextual backdrop for the analysis of the fly's flight dynamics. The tradeoff between sensory delay and information content is illustrated by the neural architecture for the haltere and visual systems shown in Figure 1.1.

1.1.1   Visual system

Given the problems that processing delays pose and the high performance and robust flight behavior observed in flies, it is of little surprise that flies have a number of evolutionary specializations that reduce sensorimotor latency. Features of the fly visual system include an elevated flicker fusion frequency, approaching 300 Hz in some cases (Autrum, 1958), as well as a unique neural superposition architecture that allows for fast response sensitivity without the normally associated loss in spatial resolution (Braitenberg, 1967). These factors make for one of the fastest visual systems in the animal kingdom, yet, visual to motor delays are still roughly 30 ms in house
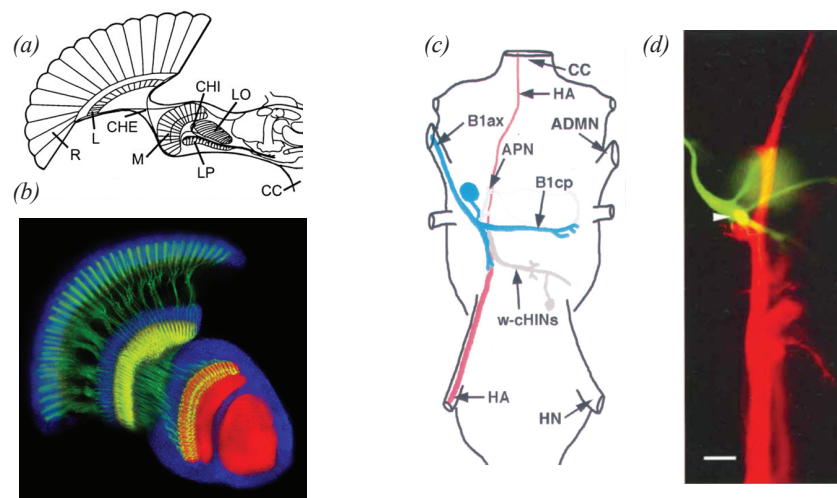
Figure 1.1: A comparison of the neuroanatomy of haltere and visual systems. *(a)* Schematic (modified from Krapp et al., 1998) and *(b)* confocal image (reproduced from Williamson et al., 2010) of a horizontal section through the *Drosophila* visual system. The retina (R) and the three visual neuropiles (lamina (L), medulla (M), and lobula complex (LP and LO)) are shown. The lamina and medulla are connected via the external chiasm (CHE) and the internal chiasm (CHI) resides between the medulla and lobula Complex. *(c)* Schematic (reproduced from Trimarchi and Murphey, 1997) and *(d)* image (reproduced from Chan and Dickinson, 1996) depicting the monosynaptic connection of the haltere afferent and the b1 (steering muscle) motor neuron.

flies (Land and Collett, 1974) and 30-40 ms in Drosophila (Hardie and Raghu, 2001; Heisenberg and Wolf, 1988; Roth et al., 2012), slower than the timescale of body dynamics during rapid saccades and other flight behaviors (Fry et al., 2003; Bender and Dickinson, 2006a).

The biophysical process of phototransduction in photoreceptor cells that converts photons into changes in membrane potential is one reason for the longer delay relative to mechanosensory counterparts (Hardie and Raghu, 2001). Additionally, extracting behaviorally relevant information requires processing which takes place in several distinct layers of neuropile in the visual system. There is a large body of literature describing the behavioral and physiological responses of the dipteran visual system (Götz, 1975; Egelhaaf and Borst, 1993; Krapp, 2000) as well as its anatomical and functional organization (Strausfeld, 1984). A brief description is provide here. The compound eye consists of a hexagonal lattice of roughly 700 ommatidia (Heisenberg and Wolf, 1984), which are individual subunits containing photoreceptors. The retinotopy of information collected from the photoreceptors is maintained through several layers of neuropile as signals progress from the lamina to the medulla via the external chiasm and then onto the lobula complex, which is composed of the lobula and lobula plate (Krapp et al., 1998). A schematic is shown in Figure 1.1. Signals from small-field elements are spatially integrated by lobula plate tangential cells (LPTCs), a collection of about 60 visual interneurons (Hausen, 1993). The post synaptic targets of the LPTCs are mostly descending neurons that project to various motor centers. A sub-population LPTCs called the vertical system (VS) and horizontal system (HS) cells, named for their directional sensitivity and morphological orientation, have notable responses to wide-field optic flow and are thought to be important in optomotor responses. The VS and HS cells integrate input received from local correlation-based movement detectors, but a mapping of their receptive fields shows a local motion preference consistent with optic flow fields expected from particular self motion components. The matched filter hypothesis suggests that these visual interneurons are optimally tuned to an optic flow field generated by motion about a specific axis and are therefore able to generate a response to rotations that is largely independent

of translation (Krapp, 2000). Estimating translational egomotion quantities would require some intrinsic assumptions about the average distance and distribution of objects in the environment (Fry et al., 2009; Taylor and Krapp, 2008), but an absolute estimate of velocity may not be necessary for successful navigation and control tasks such as approaching a post for landing (Van Breugel and Dickinson, 2012).

1.1.2 Halteres

The halteres, which are unique to dipterans, provide feedback on a much shorter timescale than is possible with the visual system (Dickinson, 1999; Ristroph et al., 2010; Bender and Dickinson, 2006a). In addition to providing timing input for synchronous flight control muscle (Heide, 1983; Dickinson and Tu, 1997), a subset of mechanoreceptors at the base of the haltere are thought to encode rotation rate by detecting strain induced by Coriolis forces. Low latency spike responses to mechanoreceptors (Fox and Daniel, 2008), and direct electrical synaptic input to steering motor neurons from haltere afferents bypassing the thoracic neuropile (Chan and Dickinson, 1996; Trimarchi and Murphey, 1997; Fayyazuddin and Dickinson, 1996), provide evidence that the haltere-motor pathway is optimized for expediency. In *Calliphora*, the total sensor-to-motor feedback delay is estimated to be approximately 3 ms (Mielke and Heide, 1993; Fayyazuddin and Dickinson, 1996), or roughly 1/2 a wing stroke period. Given that time constants on the order of 3 wing beats have been readily observed in the yaw rate body dynamics of fruit flies (Fry et al., 2003), such delays remain significant and should be handled explicitly in any flight control model (Aström and Murray, 2010).

The importance of the halteres' role in flight control was noted as early as the 18th century by Derham during ablation experiments in which he observed flies were no longer able to sustain stable flight after the removal of the halteres (1714). The halteres are small drumstick shaped organs that undergo large amplitude oscillations in a single plane in opposing phase with the wings. They evolved from the hind wings, and, despite their evolutionary derivation, serve no direct aerodynamic function. Der-

ham originally postulated that flies used their halteres much like a high-wire artist would use a balancing pole. Given their mass and stalk length, the halteres would be virtually useless in such a scenario (Pringle, 1948). With negligible contributions to both aerodynamic force production and posturing, it's curious why the halteres should have such a profound impact on flight stability. It was Pringle who proposed the modern explanation of the halteres' role in flight stability. Pringle noted that the halteres would be sensitive to Coriolis forces and thus were able measure rotation rates, providing a vibrating gyroscope for the fly (1948). The large stroke amplitude, increased stalk length, and a concentrated mass distribution at the end of the stalk where the velocity is largest are all suggestive of a morphology that has evolved for maximal sensitivity to such inertial forces. The Coriolis force is dependent on the cross-product of the haltere's linear velocity and the angular velocity of the body, meaning that strains at the haltere base would be induced both normal to the haltere stroke plane and radially. The radial strains due to Coriolis forces would be overwhelmed by the inertial forces generated from the normal haltere stroke, but the strains normal to the stroke plane would be detectable with suitably tuned sensors. Nalback simulated the normal component of Coriolis forces generated by rotations through linear mechanical oscillations and confirmed Pringle's assertion (1994). Several arrays of mechanoreceptors at the base of the haltere are strain sensitive, of which the dF2 field is both positioned correctly to measure strains normal to the stroke plane and has been shown to make a monosynaptic connection with the first basalare steering muscle (b1) motor neuron (Trimarchi and Murphey, 1997; Chan and Dickinson, 1996; Fayyazuddin and Dickinson, 1996). Further, the timing of b1 muscle activation strongly influences cycle-by-cycle changes in wing kinematics (Tu and Dickinson, 1994, 1996; Balint and Dickinson, 2004, 2001) and flies exhibit robust compensatory wing kinematic changes in response to mechanical rotations (Dickinson, 1999; Sherman and Dickinson, 2003). The low latency of the haltere feedback enables hard-wired equilibrium reflexes that may provide aerodynamic damping through rotation rate feedback (Elzinga et al., 2012). The idea that haltere feedback provides the additional damping required to stabilize flight is consistent with the observation that
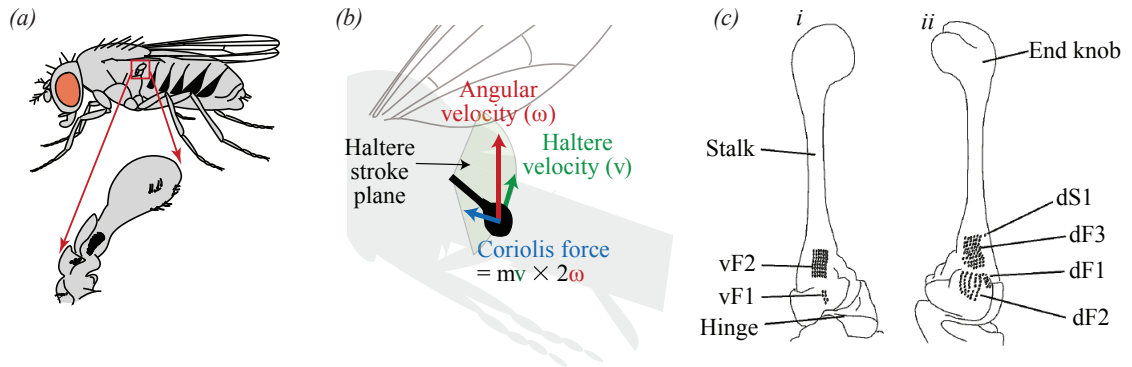
Figure 1.2: The halteres. *(a)* Diagram of the halteres and their position on the thorax behind the wings (modified from Bender and Dickinson, 2006a). *(b)* Coriolis forces deflect the haltere out of its stroke plane (modified from Bender and Dickinson, 2006a). *(c)* Morphology of the haltere (modified from Pringle, 1948) illustrating the arrays of strain sensitive campaniform sensilla on the *(i)* ventral and *(ii)* dorsal sides of the haltere.

adding a cotton thread to the abdomen restores stability after ablating the halteres (Fraenkel, 1939), thus trading active damping for passive damping.

1.1.3   Multimodal sensory integration

In flies, and other animals, feedback from numerous sensory modalities converge to facilitate complex behaviors. Flies utilize multiple sensory systems not only to take advantage of the different types of sensory information available, but to complement the response bandwidth associated with a given modality. For example, haltere afferents make connections to neck motor neurons and the head consequently shows robust compensation to body rotations, indicating a gaze stabilization reflex (Hengstenberg, 1988). This suggest that flies utilize faster sensory systems to minimize retinal blur and obtain better visually-based state estimates. This reflex is not limited to haltere feedback, however, as the compound eyes, ocelli, and halteres all contribute to com-

pensatory head movements (Hengstenberg, 1991). In addition to the haltere signals influencing what the visual system sees through compensatory head movements, visual motion has been shown in blowflies to influence the halteres through activation of haltere control muscles (Chan et al., 1998). This suggests that visual input might influence wing kinematics indirectly by co-opting the haltere reflex, which would be a convenient way to activate steering muscles in a manner appropriate for the phase of the wing stroke. Other notable examples of sensory integration include the modulation of postsynaptic targets of the VS cells based on ocellar input (Parsons et al., 2006) and the use of mechanosensory systems to aid the visual system during fast maneuvers and disturbances, such as haltere feedback during saccades (Bender and Dickinson, 2006a) and antennae-mediated feedback of airspeed changes during wind gusts (Fuller, 2011). The large number of sensory inputs relative to the number of flight control muscles, the complex interconnection of the different sensory feedback loops and the disparate nature of processing timescales involved make the fly an informative model for studying sensory fusion. For a more complete review of this topic see Taylor and Krapp (2008) or Frye (2010).

1.1.4 Flight musculature

Flies have evolved an elegant flight musculature organizational scheme where gross force production and fine dynamic control are separated into two functionally and anatomically distinct muscle groups (Dickinson and Tu, 1997). Understanding this organization provides insight into the strategies available for flight control and the actuator bandwidth constraints that the fly is subject to. The elevated power requirement for flight is generated by stretch activated asynchronous muscles running dorso-ventrally (DVMs) and longitudinally (DLMs) that fill most of the thoracic volume. These muscles do not insert into the wing base but instead induce small strains in the thorax. The orthogonality of the DVMs and DLMs means that when one set contracts, the resulting deformation of the thorax causes the other set to stretch and subsequently contract, turning the thorax into a mechanical resonator (Dickinson,

2006). Asynchronous muscle trades some sacroplasmic reticulum for myofibrils within the fiber volume resulting in greater mechanical work output at the cost of response time to neural activation, making these muscles ideal for power generation, but incapable of performing wing stroke modulations on a time scale suitable for active flight control in insects (Josephson et al., 2000). The small strains in the thorax generated by the indirect flight muscles are translated into large sweeping motions of the wing through the elaborate transmission system of the wing hinge. The precise control over the wing stroke is left to the approximately 18 pairs of synchronous muscle that insert directly on the elements of the wing hinge (Dickinson, 2006). Electrophysiological and high-speed video recordings of tethered flight in flies have correlated changes in wing kinematics with activity in these "steering" muscles (Balint and Dickinson, 2001, 2004; Tu and Dickinson, 1994, 1996). The three largest of these, b1, b2, and I1 (nomenclature from (Heide, 1983)) can explain a wide range of observed wing stroke changes (Balint and Dickinson, 2001). Muscles can function in a variety mechanical roles such as struts, springs, and dampers meaning that the steering muscles may serve to modulate of the process dynamics of the wing hinge transmission system to enact active control over the wing stroke (Dickinson et al., 2000). The b1 steering muscle, for example, behaves as a variable stiffness spring that can be controlled on a stroke-by-stroke basis (Tu and Dickinson, 1994, 1996).

1.1.5 Responses to mechanical and visual stimuli in behaving animals

The response of individual stroke features, most notably stroke amplitude and stroke frequency, to a variety of visual and mechanical stimuli have been studied extensively in tethered flight (Frye and Gray, 2005). These quantities can be tracked with an optical wing-beat analyzer which allows for a robust measure of behavioral output without the labor intensive analysis of high-speed cine that was required prior to the advent of modern high-speed video and automated machine-vision based tracking (Götz, 1987). This technique, as well as measuring yaw torque directly, in the

presence of simulated motion led to extensive characterization of optomotor reflexes in flies (Heisenberg and Wolf, 1984). Optomotor reflexes can be generally thought of as a steering response in the direction of wide-field visual motion. This steering response manifests in the wingbeat analyzer as differences in wingstroke amplitude between the left and right wing (ΔWBA). Indeed recordings of steering muscle activity showed changes in response to visual stimuli (Heide, 1983) which were later shown to account for stroke amplitude changes (Balint and Dickinson, 2001). There is a strong correlation between yaw torque and ΔWBA even though an analysis of the aerodynamic forces generated from such a change in kinematics would not suggest the relationship. Stereotyped and coordinated changes of multiple wingstroke parameters allows ΔWBA to serve as proxy for yaw torque (Balint and Dickinson, 2004; Tammero et al., 2004).

Given the robust nature of multisensory feedback and multimodal integration, it is difficult to tease apart the mechanosensory response to rigid body rotations from the visual response. Dickinson measured haltere-mediated compensatory reflexes by tethering the animal in the center of an LED visual simulator mounted within an actuated gimbal in an attempt to uncouple mechanical oscillations from the visual surround (Dickinson, 1999). In follow-up experiments, Sherman compared haltere-mediated responses to mechanical oscillations with visually-mediated responses to wide-field oscillations of the visual display pattern (Sherman and Dickinson, 2003). From these data (shown in Figure 1.3) in conjunction with an estimate of the calibration between yaw torque and ΔWBA (Tammero et al., 2004) we can infer a transfer function between measured yaw rate and actuation torque for both the visual system and the haltere system. This estimate will prove useful for the analysis in Chapter 2. Further, Sherman was able to show in a subsequent paper that it is appropriate to superimpose haltere- and visually-mediated responses (Sherman and Dickinson, 2004).
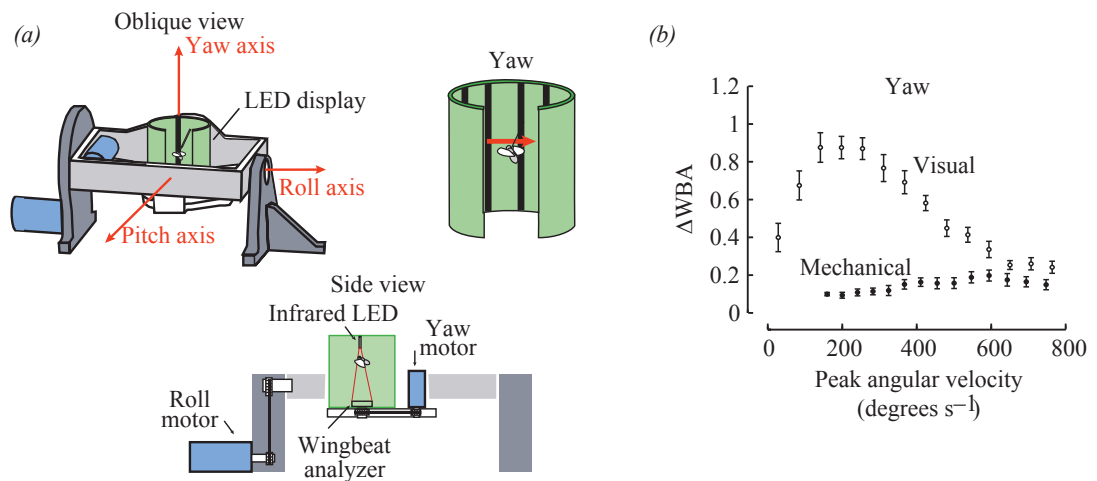
Figure 1.3: Visually- and haltere-mediated responses to yaw oscillations. (a) Flight simulator apparatus. (b) ΔWBA response as a function of stimulus peak angular velocity. Experiments were carried out with a fixed angular position amplitude meaning that stimulus frequency would increase with increasing peak angular velocity (schematic and data from Sherman and Dickinson, 2003).

1.2   Kinematics and flapping wing aerodynamics

1.2.1   Wing kinematics

Fruit flies sweep their wings back and forth at a high angle of attack, rapidly rotating at the end of the upstroke and downstroke so that lift is produced during both half-strokes (Zanker, 1990; Ellington, 1984b). The wingtip traces out a gentle u-shape when projecting the trajectory onto a plane bisecting the thorax longitudinally (Dickinson, 2006). The convention used in this dissertation follows after Sane (2001) and describes the wing position as set of Euler angles defined in Figure 1.4. The stroke angle (ϕ) describes the primary and back and forth motion. The deviation angle (θ) describes the elevation of the wing out of the stroke plane. Finally, the rotation angle (α) describes the spanwise pitch angle of the wing. In the crudest description of the wing kinematics of a fruit fly, the stroke angle follows a triangle wave with peak-to-peak amplitude of approximately 140 degrees, the deviation angle is negligible, and the rotation angle follows a square wave which provides a 45 degree angle of attack at mid-stroke. In reality the stroke angle is roughly in between a pure sinusoid and triangle wave, the deviation angle is small throughout the stroke but has significant frequency content in the first two Fourier components, and the rotation angle also has significant frequency content at twice the wing beat frequency. Wing kinematic descriptions based on stroboscopic photography and high-speed video are given by Ellington (1984b), Zanker (1990), and Fry (2003). A more theoretical treatment based on optimal kinematics for energy minimization is provided by Berman and Wang (2007).

Numerous studies have been carried out to identify the changes in wing stroke kinematics responsible for flight stabilization, subtle course corrections, and active maneuvers. Whereas changes in stroke amplitude and frequency have been correlated with body forces and torques, the vast array of flight maneuvers of which fruit flies are capable suggest these parameters alone are not enough to provide the necessary control authority and a more detailed kinematic analysis is required. Access to time resolved comprehensive kinematic variables is generally achieved through the
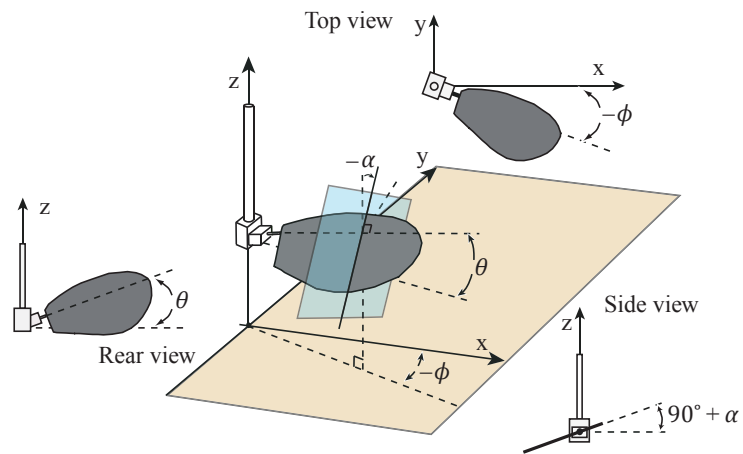
Figure 1.4: Euler angle convention describing wing kinematics of flapping flight. ϕ is the stroke angle, θ is the deviation angle, and α is the rotation angle (modified from Dickson and Dickinson, 2004).

labor intensive digitization of high speed video sequences and its precursor strobo-
scopic photography. Vogel made observations of tethered Drosophila in a wind tunnel
using stroboscopic photography, which pointed to kinematic parameters involved in
lift and thrust variation (1967). Advances in high-speed videography, including the
increased spatial and temporal resolution as well as mature methods for calibrating
multiple camera views have yielded more detailed descriptions of tree dimensional
wing kinematics (Fry et al., 2003). In larger flies, Balint was able to describe several
stereotyped wing tip trajectories and attribute them to specific patterns of activity in
specific synchronous flight control muscles, suggesting a coupling of several kinematic
variables during a flight maneuver (2001; 2004). It remains unclear the degree to
which flies have independent control over any specific kinematic parameter or even
which parameters are the most important from a controllability standpoint. Recently
developed machine-vision-based automated tracking systems designed for free flight
allow for higher throughput in more naturalistic conditions and will hopefully serve
to elucidate these issues (Fontaine et al., 2009; Ristroph et al., 2009).

1.2.2 Measuring aerodynamic forces

Dynamically-scaled physical models, computational fluid dynamics (CFD), and quasi-
steady modeling have allowed researchers to assess the role of wingstroke parameters
in aerodynamic force production, either through the playing out of measured wing
kinematics or through the use of simplified conceived kinematics designed to isolate
specific features (Ramamurti and Sandberg, 2007; Hesselberg and Lehmann, 2007;
Dickson et al., 2008, 2010; Cheng et al., 2010; Sane and Dickinson, 2001). Each
method for obtaining aerodynamic forces and moments from wing and body kine-
matics has inherent advantages and disadvantages (for reviews see Sane, 2003; Shyy
et al., 2010). Quasi-steady modeling assumes the instantaneous lift and drag forces
can be approximated by the steady-state forces acting on the wing with equiva-
lent velocity and angle of attack relative to the free stream. Often the quasi-steady
assumption is used in conjunction with blade-element theory to create models of

flapping wing aerodynamics. Flapping flight is inherently unsteady and the result-
ing unsteady mechanisms are essential to explaining how sufficient lift is generated
to maintain weight support (Ennos, 1989; Ellington, 1984a; Dickinson et al., 1999;
Ellington et al., 1996; Maxworthy, 1979, 1981). Flies, and many other insects, sweep
their wings at high angles of attack, developing a leading edge vortex (LEV). Whereas
in traditional steady-state theory this vortex would repeatedly develop, grow unsta-
ble and shed, leading to a stalling condition, the LEV is stabilized by axial flow and
remains attached during the revolving stroke of a fly wing, thus enhancing force pro-
duction (Lentink and Dickinson, 2009; Dickinson et al., 1999; Ellington et al., 1996;
Maxworthy, 1981). Additionally, the wing repeatedly moves through its own wake
upon stroke reversal which implies that the animal could recover some of the energy
lost to the wake from the previous stroke (Dickinson et al., 1999). A number of other
unsteady phenomena, including added mass, rotational circulation, and the clap-and-
fling, also contribute to the aerodynamic forces of flapping flight (for review see Sane,
2003).

Despite the importance of unsteady mechanisms in insect flight, quasi-steady
models still have utility. Quasi-steady-based models have high degree of flexibil-
ity are much less computationally intensive than 3D CFD-based models, allowing for
rapid exploration of the parameter space. Researchers have had success with aug-
menting quasi-steady-based expressions with empirically measured coefficients from
dynamically-scaled models to capture some of unsteady effects (Dickson et al., 2008;
Faruque and Humbert, 2010a,b). Although such a technique masks the unsteady
features hidden within these coefficients, these models perform reasonably well for
stroke-averaged simulations.

Dynamically-scaled models have proven useful for studying unsteady mechanisms
in insect flight, but they are more difficult to incorporate into simulations of the body
dynamics than numerical methods. Carrying out such experiments on a dynamically-
scaled model requires a special type of robotics, called captive trajectory systems.
Captive trajectory systems measure the applied forces on the object of interest, run
these forces through the equations of motion, and actuate the body appropriately

in real-time under closed-loop conditions. For the study of flapping flight, such a system would entail measuring forces and moments on the airframe of a dynamically scaled robot, integration of the rigid body equations of motion, and rotating and/or translating the airframe, thus allowing the model to "fly itself" and provide an environment for the systematic study of free-flight dynamics. In addition to providing experimental flexibility, this method allows the inertia to be properly scaled for the robot, which would not be readily achievable for a purely physical implementation.

1.3 Stroke-averaged models

Through the synthesis of time-resolved wing and body kinematics in both tethered and free-flight conditions (Fry et al., 2003; Ristroph et al., 2009; Zanker, 1990) and the measurement of the corresponding aerodynamic forces and moments by means of dynamically-scaled models, computational fluid dynamics, or quasi-steady estimates (Ellington, 1984a; Sane, 2003; Ramamurti and Sandberg, 2007; Dickinson et al., 1999; Cheng et al., 2010), researchers have constructed flight dynamics models aimed at understanding both the underlying passive dynamics of flapping flight as well as the requirements and strategies for stabilization and control (Cheng et al., 2011; Faruque and Humbert, 2010a; Sun and Xiong, 2005; Gao et al., 2011; Sun and Wang, 2007; Ristroph et al., 2010; Dickson et al., 2008; Cheng and Deng, 2011). The general technique for composing such models is standard practice in the aircraft literature and consists of measuring aerodynamic forces and moments in response to perturbations about an equilibrium flight condition to construct a matrix of stability derivatives and subsequently determine the dynamic modes of the linearized system through its eigenvalues (Etkin and Reid, 1998). A linearized state-space model of insect flight dynamics provides a convenient framework for addressing flight control questions. This approach was first used in the context of insect flight for locusts where the forces and moments were measured directly on a tethered animal and averaged over the stroke period (Taylor, 2003). In later studies, stroke-averaged linear models were derived from computational methods and dynamically-scaled physical models for bees,

flies, and moths, a few of which considered forward flight (Epstein et al., 2007; Sun and Wang, 2007) whereas the majority focused on hovering conditions (Faruque and Humbert, 2010a; Sun and Xiong, 2005; Xiong and Sun, 2007; Gao et al., 2011; Cheng and Deng, 2011). All of these models identified at least one unstable mode, which highlights the importance of feedback-based modulation of the wing kinematics to achieve stable flight.

1.3.1 Justification

The periodic nature of flapping flight leads to small fluctuations superimposed on a course trajectory. Often the behavior of this course trajectory is of greater interest and can be analyzed by treating the higher frequency forcing functions as their average over the forcing period, an idea that is formalized in averaging theory (for a complete treatment see Khalil, 1996). Several follow-up studies in insect flight dynamics have considered dynamics models that take into account the periodic nature of flight forces associated with flapping flight (Taylor and Zbikowski, 2005; Wu and Sun, 2012), but stroke-averaged models are still appropriate at the spatial and temporal scale of *Drosophila* flight dynamics (Dickson et al., 2010; Wu and Sun, 2012). Wu and Sun (2012) performed a Floquet stability analysis on the flapping flight dynamics of the dronefly and showed that the results were in close agreement with a stroke-averaged analysis. Dickson et al. (2010) performed system identification tests with a dynamically-scaled robot under captive trajectory that confirmed that a linear stroke-averaged model accurately captures the essential dynamics of the system on timescales larger than several wing strokes (Dickson et al., 2010), the results of which are provided in Figure 1.5. Averaging theory often takes advantage of a separation of timescales between high frequency forcing and the relatively slow timescale of the body dynamics. This makes sense from a linear systems perspective in that a low bandwidth system would attenuate a high frequency input. Although linear systems theory provides the proper intuition, the validity of averaging theory does not rely on the linearity of the system (Khalil, 1996).
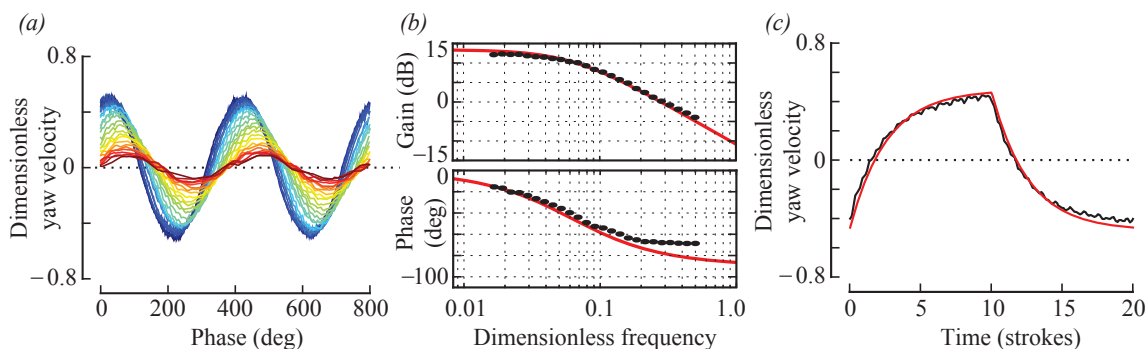
Figure 1.5: Yaw velocity system response to asymmetric shifts in wing rotation angle kinematics for a dynamically scaled robot in captive trajectory (data from Dickson et al., 2010). *(a)* Response to sinusoidal inputs. *(b)* Bode plot. *(c)* Square wave response.

1.3.2   Hovering yaw turns

During fast yaw turns, known as saccades, which are characteristic to fly flight, inertia was thought to dominate based on high-speed video of free flight yaw turns and an estimate of body damping using Stokes-law (Fry et al., 2003). This would mean that the deceleration at the end of the turn would have to be generated actively from changes in kinematics with little contribution from body drag. A number of kinematic parameters have been studied as modes of generating yaw torque (Dickson et al., 2010), but asymmetries in angle of attack between the two wings have accumulated the most support in the literature (Ristroph et al., 2009, 2010; Dickson et al., 2010; Humbert and Faruque, 2011). As was mentioned previously, there is a very strong correlation between ΔWBA and yaw torque, but this is more of a testament to the coordinated nature of changes among wing kinematic parameters than a suggestion that ΔWBA generates yaw torque.

Researchers later observed that drag would not be limited to the body but would be present on the wings as well. Further, the additional forces due to body motion

were best interpreted separately from the forces generated by the wings during a stroke. Under quasi-steady assumptions, this stroke-averaged yaw torque is expected to be linear with respect to yaw rate (Hesselberg and Lehmann, 2007; Hedrick et al., 2009). An asymmetry in drag between the left and right wings on both the upstroke and the downstroke due to yaw rotations leads to quadratic terms that drop out and a damping term that is linear in yaw rate. This result extends to the unsteady case as shown by studies using dynamically-scaled robots (Dickson et al., 2010; Cheng et al., 2010). Yaw damping due to the additional aerodynamic forces on wings from body rotation is roughly two orders of magnitude larger than the damping due to just the body. This led some researchers to posit that the angular deceleration phase of yaw turns in flying animals is entirely mediated by passive damping (Hedrick et al., 2009). Dynamically-scaled robotic experiments and computational methods have shown that aerodynamic damping in flapping flight is indeed important to the dynamics of yaw turns (Dickson et al., 2010; Cheng et al., 2010; Hesselberg and Lehmann, 2007), but active changes in wing kinematics and feedback-based responses likely play an important role as well.

1.3.3 Forward flight

Previous researchers concluded that the regulation of forward flight speed, a critical task for successful navigation, was governed by a simple inverse relationship with body pitch (Vogel, 1966). Free-flight wind-tunnel experiments with *Drosophila* (David, 1978; Medici and Fry, 2012) as well as tethered force measurements indicating that the animals will only alter the magnitude but not the elevation of their stroke-averaged flight force vector in response to longitudinal visual stimuli (Götz and Wandel, 1984), provided evidence for this hypothesis. Further, stroke plane inclination does not change significantly in *Drosophila* with visual pattern motion (Götz and Wandel, 1984). Consequently, the flight motor in flies is often described as an actuator disk with a fixed orientation with respect to the body. In this model, forces are redirected by means of changes in body pitch, and force production is regulated by wingstroke

amplitude and to a lesser degree, wingstroke frequency (Vogel, 1966, 1967; David, 1978; Lehmann and Dickinson, 1997; Götz et al., 1979). As it appears that the underlying morphology is capable of much more complex patterns of wing motion, researchers attributed the fixed inclination of the flight force to the benefits of a simple control scheme.

The means by which animals regulate and stabilize forward flight via changes in wing and body kinematics remains an active area of research (Sugiura and Dickinson, 2009; Xiong and Sun, 2007; Ristroph et al., 2011). Recent high-speed video analysis of forward flight sequences in fruit flies has suggested that upstroke-to-downstroke shifts in the spanwise rotation angle of the wing play an instrumental role in forward propulsion (Ristroph et al., 2011). This theme was echoed in work on the dynamics of backwards pitching maneuvers in hawkmoths (Cheng et al., 2011). Through a variety of evidence in both tethered and freely flying fruit flies, previous experimenters had concluded body attitude and a corresponding shift in the mean stroke position were primarily responsible for dictating equilibrium flight speed (Vogel, 1966; David, 1978; Götz and Wandel, 1984; Zanker, 1988). These two ideas are not necessarily contradictory, but a more complete theoretical treatment might be helpful in forming a consistent synthetic model.

1.4 Contributions

This thesis explores the relationship between active compensatory feedback and the underlying passive flight dynamics in *Drosophila*, the fruit fly, in light of the constraints imposed by sensorimotor delays and the sensory systems available to the fly. The mathematical and experimental tractability of yaw turns during hovering, along with the vast body of literature regarding visual- and mechanosensory-mediated responses to rotatory stimuli has made the study of wing kinematics governing such maneuvers an excellent entry point into the problem (Ristroph et al., 2010; Fry et al., 2003; Hedrick and Robinson, 2010; Iriarte-Díaz and Swartz, 2008) and is where Chapter 2 begins. In Chapter 3, I move on to the study of forward flight dynamics where

general themes begin to emerge on the role of mechanosensory reflexes in the over-
all architecture of flies' flight control circuitry. This work is primarily based on two
journal articles and the specific contributions of my co-authors to these papers are
documented in the acknowledgments (Elzinga et al., 2012, In review).

1.4.1 The influence of sensory delay on the yaw dynamics of flapping flight

In Chapter 2, I explore the effect of feedback delay on the stability and performance
of a proportional yaw rate controller in the context of a stereotyped body saccade of
a fruit fly, in which the animal performs a rapid turn of approximately 90° in 50 to
100 ms (Tammero and Dickinson, 2002; Bender and Dickinson, 2006b). To perform
this analysis, we utilized a dynamically-scaled robotic model with captive trajectory
capability about the yaw axis. Yaw torque was controlled through a bilateral asym-
metry in angle of attack, which has been observed in yaw turns of real flies and used
in previous studies (Bergou et al., 2009; Dickson et al., 2010). We studied step and
impulse responses in yaw velocity with the robot under proportional control for a
range of feedback delays similar in dimensionless timescale to those present in the
nervous system and compared these responses to stroke-averaged simulations. The
results demonstrate that proportional control decreases the system time constant by
adding an active damping component, but is constrained by a tradeoff between sensor
delay and permissible feedback gain. This suggests that the role of the haltere may
be to provide fast inner-loop feedback, resulting in additional active damping that
would allow the slower visual system to operate at higher gain with a faster response
for the same level of robustness. The experiments also provide evidence that the
large open-loop responses observed in tethered-flight might not be an artifact of the
preparation, as previously suggested (Taylor et al., 2008), but are indeed what would
be required of a well-tuned flight control system.

1.4.2 Wing kinematics and the stabilization of longitudinal forward flight

In Chapter 3 I utilize a dynamically-scaled robotic model to explore the longitudinal flight dynamics for flies in level forward flight. We measured the flight forces and moments during constant translational velocity moves over a range of applicable body pitch angles for a baseline set of hovering kinematics. These data allowed us to construct models to assess flight stability and determine the requisite trim forces, providing, to our knowledge, the most comprehensive characterization of forward flight dynamics in flies to date. The nature of the force deficit provides insight into the changes in wing kinematics that may be utilized by the animals to achieve steady forward flight. We considered three different deformations of hovering wing kinematics, which were inspired by previous experimental studies and that result in the generation of a pitch moment: a shift in the mean stroke position, upstroke-to-downstroke differences in wing rotation angle, and upstroke-to-downstroke differences in stroke deviation (Vogel, 1967; Ristroph et al., 2011; Balint and Dickinson, 2004). The results suggest potential roles for each of the deformation modes in trimming flight forces and stabilizing the dynamics of level forward flight in flies. The mean stroke position of the flapping wings is a likely candidate for trimming the pitch moment at all speeds, whereas changes in the wing rotation angle are required only at high speeds. This leads to a possible reconciliation of opposing hypotheses regarding the mechanism for forward propulsion in flies, which were proposed based on previous tethered flight experiments and recent free-flight experiments. The results also show that the dynamics may be stabilized with the addition of a pitch damper, but that the magnitude of required damping increases with flight speed. We posit that differences in stroke deviation between the upstroke and downstroke, which is an often neglected wing stroke parameter, might play a critical role in this stabilization. Fast mechanosensory feedback of the pitch rate could enable active damping, which would inherently exhibit gain scheduling with flight speed if pitch torque is regulated by adjusting stroke deviation. Such a control scheme would provide an elegant solution

for flight stabilization across a wide range of flight speeds.

Chapter 2

The influence of sensory delay on the yaw dynamics of flapping flight

Flapping-wing insects fly with unprecedented maneuverability and stability compared with conventional aircraft.

—Bo Cheng (2011)

2.1   Summary

In closed-loop systems, sensor feedback delays may have disastrous implications for performance and stability. Flies have evolved multiple specializations to reduce this latency, but the fastest feedback during flight involves a delay that is still significant on the timescale of body dynamics. We explored the effect of sensor delay on flight stability and performance for yaw turns using a dynamically scaled robotic model of the fruit fly, *Drosophila*. The robot was equipped with a real-time feedback system that performed active turns in response to measured torque about the functional yaw axis. We performed system response experiments for a proportional controller in yaw velocity for a range of feedback delays, similar in dimensionless timescale to those experienced by a fly. The results show a fundamental tradeoff between sensor delay and permissible feedback gain, and suggest that fast mechanosensory feedback in flies, and most likely in other insects, provides a source of active damping that compliments that contributed by passive effects. Presented in the context of these findings, a

control architecture whereby a haltere-mediated inner-loop proportional controller provides damping for slower visually-mediated feedback is consistent with tethered-flight measurements, free-flight observations, and engineering design principles.

2.2 Materials and methods

2.2.1 Robotic fly apparatus

Experiments were conducted in a 1m × 2.4m × 1.2m tank of mineral oil (Cheveron Superla white oil; Chevron Texaco Corp. San Ramon CA, USA; density $880\mathrm{kg}\cdot\mathrm{m}^{-3}$, kinematic viscosity 115 cSt at 25°C) using a dynamically-scaled model of Drosophila with hardware identical to the apparatus described previously (Dickson et al., 2010). We will briefly reiterate this description for convenience as well as highlight the additional capabilities enabled by a software redesign. The robot consists of two isometrically-scaled acrylic wings (length (R) = 230 mm, mean chord $(\bar{c})$ = 65 mm, width = 2.3 mm), each with three independently actuated degrees of freedom: stroke angle (ϕ), deviation angle (θ), and rotation angle (α), as illustrated in Figure 2.1. The stroke axes of the two wings were parallel and separated by 0.11 m. The wing motor assemblies were attached to a common frame which was mounted on a shaft to allow rotation about the functional yaw axis. A geometrically scaled body model was not used because the damping due to the body is roughly two orders of magnitude smaller than that of the flapping wings, and can be ignored for most studies (Hesselberg and Lehmann, 2007; Hedrick et al., 2009; Dickson et al., 2010). The stroke position of each wing was controlled by a stepper motor (M-1715-1.5D, Schneider Electric Motion, Marlborough, CT, USA) whereas the rotation and deviation positions were controlled by digital servo motors (HSC-5996TG, Hitec RCD, Poway, CA, USA). The yaw rotation of the airframe was actuated by a stepper motor (M-2218-3.0S, Schneider Electric Motion, Marlborough, CT, USA). A torque sensor (TQ202-25Z, Omega Engineering, Stamford, CT, USA; full scale range of 0.175 N-m, accuracy of 0.2 % full scale output) mounted axially between the shaft and base plate measured yaw
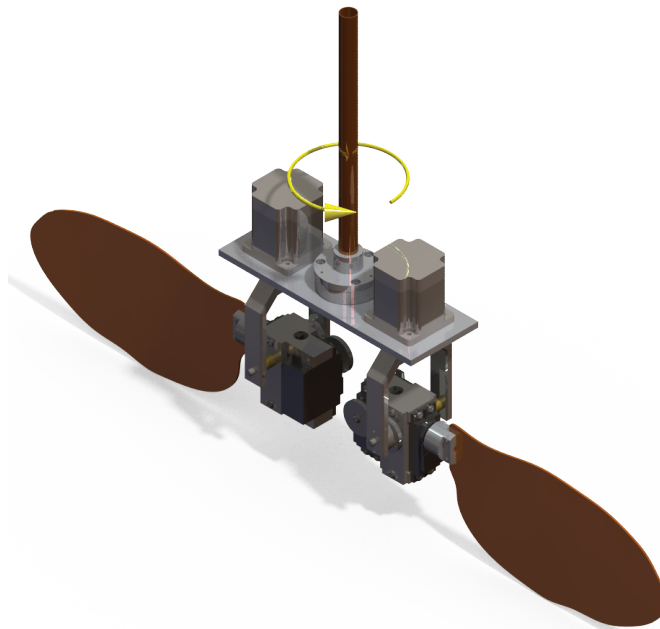
Figure 2.1: Experimental apparatus. Design drawing of the dynamically scaled robotic model. Each wing has three degrees of freedom, stroke, deviation, and rotation. Torque is measured where the base of the yaw rotation shaft meets the airframe.

torque in the body frame.

The robot was controlled using a PC running a hard real-time Linux kernel with custom software written in Python and C. At each time step within a 3 kHz real-time loop, torque generated by the aerodynamic forces on the wings was measured and passed to a model of the fly's inertial dynamics and new wing kinematics were generated based on a prescribed output-feedback controller. The state variables were held in a buffer in order to implement a virtual sensor delay. The model of the fly's inertial dynamics is given by:

$$\dot{\psi} = \omega, \tag{2.1}$$

$$I\dot{\omega} = \tau_{meas}(t) - b\omega \approx \tau_{meas}(t), \tag{2.2}$$

where ψ is the heading angle, I is the moment of inertia about the yaw axis, ω is the yaw velocity, τ_{meas} is the yaw torque measured by the sensor, and b is a velocity-dependent body damping term. This equation was integrated using the classical Runge-Kutta method (Butcher, 2008) to set the yaw velocity and heading angle of the system at each time step. For the experiments in this manuscript, the body damping term was dropped for the same reason that a physical body model was not used; the aerodynamic forces acting on flapping wings that provide damping during yaw rotation dominate the effects of body drag (Hesselberg and Lehmann (2007)). For appropriate dynamic scaling of this equation, we matched the Reynolds number (Re), dimensionless yaw velocity (ω^*), and dimensionless moment of inertia (I^*). These dimensionless quantities are defined by the following:

$$\mathrm{Re} = \frac{2R\Phi f\bar{c}}{\nu}, \tag{2.3}$$

$$\omega^* = \frac{\omega}{f}, \tag{2.4}$$

$$I^* = \frac{I}{\rho\bar{c}^5}, \tag{2.5}$$

where R is the wing length, Φ is the (peak-to-peak) stroke amplitude, f is the flapping frequency, $\bar{c}$ is the mean wing chord, ν is the kinematic viscosity, and ρ is the density of the fluid. A flapping frequency of 0.167 Hz was used to yield a Re of 100, consistent with flapping flight in Drosophila (Lehmann and Dickinson, 1997). The dimensionless moment of inertia about the functional yaw axis used in this study was 1.97×10^3, in agreement with those used in previous studies (Hedrick et al., 2009; Dickson et al., 2010). This was calculated by modeling the fly as a cylinder inclined at 55°, corresponding to a hovering flight posture. All subsequent values and equations will appear in their dimensionless form.

2.2.2 Wing kinematics

We used idealized *Drosophila* wing kinematics that utilize a differential angle of attack control mode as described previously (Dickson et al., 2010). The linearity of additional control modes studied in previous work allows us to perform these studies in the context of just one mode and apply the results generally to a desired superposition of control modes (Dickson et al., 2010). The kinematics consist of a nominal set based on previous work (Berman and Wang, 2007), augmented with an asymmetry parameter in right and left wing rotation angle as a means of generating yaw torque. The stroke position, deviation, and rotation angle for the baseline kinematics are given as follows:

$$\phi_b(t) = \frac{\phi_0}{\arcsin(k_\phi)} \arcsin[k_\phi \cos(2\pi f t)], \tag{2.6}$$

$$\theta_b(t) = 0, \tag{2.7}$$

$$\alpha_b(t) = \frac{\alpha_0}{\tanh(k_\alpha)} \tanh[k_\alpha \sin(2\pi f t)], \tag{2.8}$$

where f is the flapping frequency, ϕ_0 is the stroke amplitude, α_0 the rotation amplitude, and the parameters k_ϕ and k_α control the shape of the wing kinematics. Values of $k_\phi = 0.01$ and $k_\alpha = 1.5$ were selected to produce waveforms that resemble an idealized version of the wing kinematics of *Drosophila* (Berman and Wang, 2007; Dickson et al., 2010). Similarly, a value of $\phi_0 = 70°$ was used to give a peak-to-peak stroke amplitude of $140°$ and a value of $\alpha_0 = 45°$ was used to give a $45°$ angle of attack at mid-stroke. Because the yaw rotation axis is aligned with the stroke plane normal and no deviation is considered, the geometric angle of attack is specified by the rotation angle with an appropriate offset. The differential angle of attack mode deforms the baseline rotation angles in the following manner, leaving the other degrees of freedom unchanged:
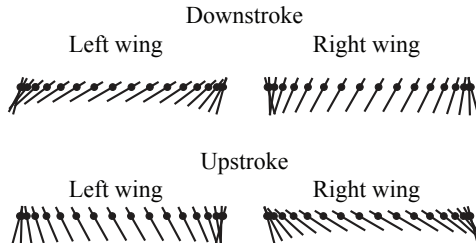
Figure 2.2: Pictorial representation of the wing kinematics, illustrating the asymmetry in wing rotation angle consistent with the differential angle of attack deformation mode described in (Dickson et al., 2010).

$$\alpha_{L,R}(t) = \alpha_b(t) \pm u, \tag{2.9}$$

where u is the deformation parameter. A nonzero value for u introduces asymmetry into the wing kinematics, as shown by example left and right wing tip trajectories in Figure 2.2. For illustrative purposes, consider a baseline angle of attack at mid-stroke of $45°$. A positive u would increase the rotation angle on the downstroke in the left wing, reducing the angle of attack and consequently the drag force while having the opposite effect on the right wing. This asymmetry would reverse on the upstroke, resulting in a net yaw torque and inducing a turn to the right.

Feedback control was enabled by generating the kinematics from within the real-time loop with a state dependent differential angle of attack deformation parameter. We implemented a simple yaw rate proportional controller with a zero set point and feedforward asymmetry, u_{ff}, by constructing u in the following manner:

$$u(t) = -k_p \omega(t) + u_{ff}(t) \tag{2.10}$$
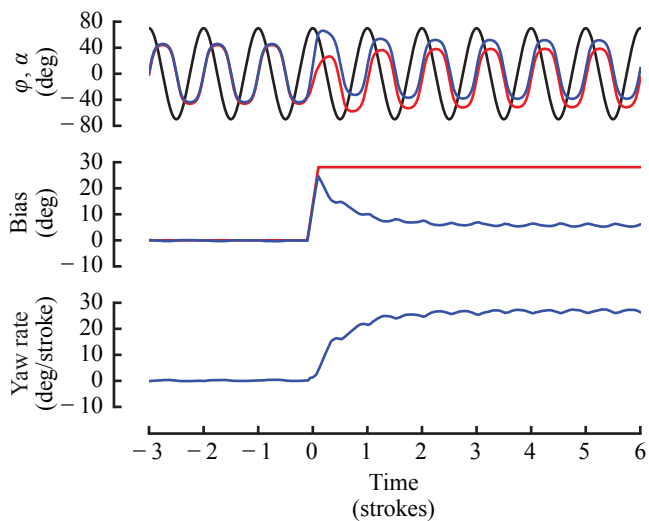
Figure 2.3: Sample data for a typical step response experiment. The kinematics shown are the stroke angle (single black curve) and the left (red) and right (blue) wing rotation angles. The commanded asymmetry in rotation angle is in red while the actual asymmetry is in blue. The bottom panel is the corresponding yaw rate response.

where k_p is the proportional feedback gain and ω is the yaw rate. The effect of each term in the controller is apparent in the sample step response shown in Figure 2.3. When considering feedback with a fixed delay this becomes:

$$u(t) = -k_p\omega(t - \delta) + u_{ff}(t) \tag{2.11}$$

where δ is the delay time. A morphological limit on the maximum asymmetry was also considered, and manifested as a software limit on the maximum value of u.

2.2.3 Stroke-averaged modeling

Simulations were carried out with code written in Python that utilized the SciPy module (Jones et al., 2010) by considering the following stroke-averaged linear dynamics:

$$I\dot{\omega} = \tau_\omega + \tau_u = -C_\omega\omega + C_u u(t), \tag{2.12}$$

where τ_ω and τ_u are the contributions to dimensionless torque from passive damping and the asymmetry parameter, u, respectively; C_ω is the damping coefficient, and C_u is the actuation coefficient. The dimensionless damping coefficient and dimensionless actuation coefficient were both experimentally determined by averaging yaw torque over 5 identical wing strokes, as measured by the robotic fly apparatus, following a similar procedure to that described previously (Dickson et al., 2010). These measurements were performed with prescribed yaw velocity in the absence of the captive trajectory system. The dimensionless damping coefficient used was 7.47×10^2 and was determined by a linear fit of the relationship between stroke-averaged yaw torque and yaw rate for a fixed value of u. The dimensionless actuation coefficient was 3.53×10^3 and was derived from the linear relationship between yaw torque and the actuation parameter for a fixed yaw rate.

In addition to including the constraint on the maximum value of u, we also modeled a saturation in the actuation torque, τ_u. Whereas the drag coefficient for a revolving wing in a Reynolds number regime near 100 is relatively linear with rotation angles near 45°, this approximation breaks down with significant deviation in rotation angle which spawns the saturation in the actuation torque. The saturation was modeled with a hyperbolic tangent function with one experimentally determined parameter, A:

$$\tau_u = \frac{1}{A}\tanh(Au)C_u. \tag{2.13}$$

The experimental parameter had a value of $A = 1.39$, and was determined by least
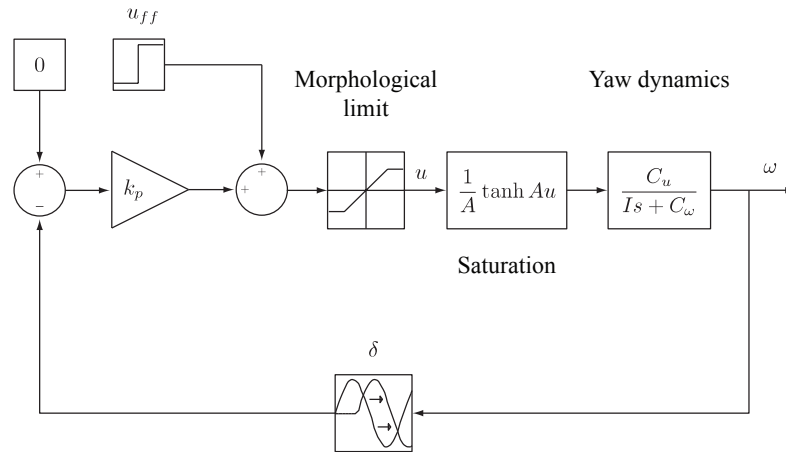
Figure 2.4: Block diagram model used for stroke-averaged simulations of a proportional yaw rate controller. The model has set point of zero and a commanded asymmetry input representing a motor command to the steering muscles. The two saturation blocks are a morphological limit on the maximum asymmetry and a saturation in the drag coefficient approximated by a hyperbolic tangent function with one measured parameter. C_u is the actuation coefficient, C_ω is the damping coefficient, and u is the asymmetry parameter. There is a fixed sensor delay, δ, in the feedback loop.

squares fit of Equation 2.13 to torque vs. u data for a fixed yaw velocity. The dynamics in Equation 2.12 can be written as a transfer function and combined with both the saturation in Equation 2.13 and the controller in Equation 2.11 to form a block diagram model of the system used to perform the simulations as illustrated in Figure 2.4.

2.3 Results

2.3.1 Step responses in the undelayed system

The role of feedback gain in determining the system time constant was explored through a series of yaw velocity step response experiments. The step was approximated by a steep ramp and hold of the feedforward command parameter, u_{ff}, with the ramp width equal to 0.20 wing strokes and temporally centered on the defined trial start time, $t = 0$. All trials were conducted in closed-loop with undelayed feedback and consisted of 5 wing beats that were bilaterally symmetric (i.e $u_{ff} = 0$) to produce fluid conditions representative of hover, followed by 10 wing beats to measure the system response to a change in the commanded input. Illustrative sample data for these trials are shown in Figure 2.3. The controller gain, k_p, was varied from 0.00 to 0.93. Higher gains were not possible because they would lead to wing kinematics that were both biologically implausible and beyond the calibration limits of the servo motors controlling rotation. A proportional controller leaves a steady-state error that is gain dependent, meaning that using the same u_{ff} value across a range of gains yields a different steady-state velocity. Although the magnitude of the step change in velocity would not affect the time constant for a linear system, we felt a more relevant comparison was to choose u_{ff} for each trial in a manner that resulted in a consistent steady-state yaw velocity of $27°\text{stroke}^{-1}$, a conservative upper limit on the peak speed during a saccade (Tammero and Dickinson, 2002; Fry et al., 2003).

Time series data for the yaw rate step responses of the robot are shown in Figure 2.5(a) and (b). The response is indicative of an approximately linear first-order system, with higher frequency oscillations, due to torque peaks generated over each half-stroke, superimposed on the response. We determined the time constant of each response by a least squares fit of a first order response to the trace. Time constants for each controller gain are plotted in Figure 2.5c with a comparison to model predictions. The time constant decreased with gain at a diminishing rate, in close agreement with model predictions.

High gain cases in which sub-wingstroke time constants were achieved, resulted in
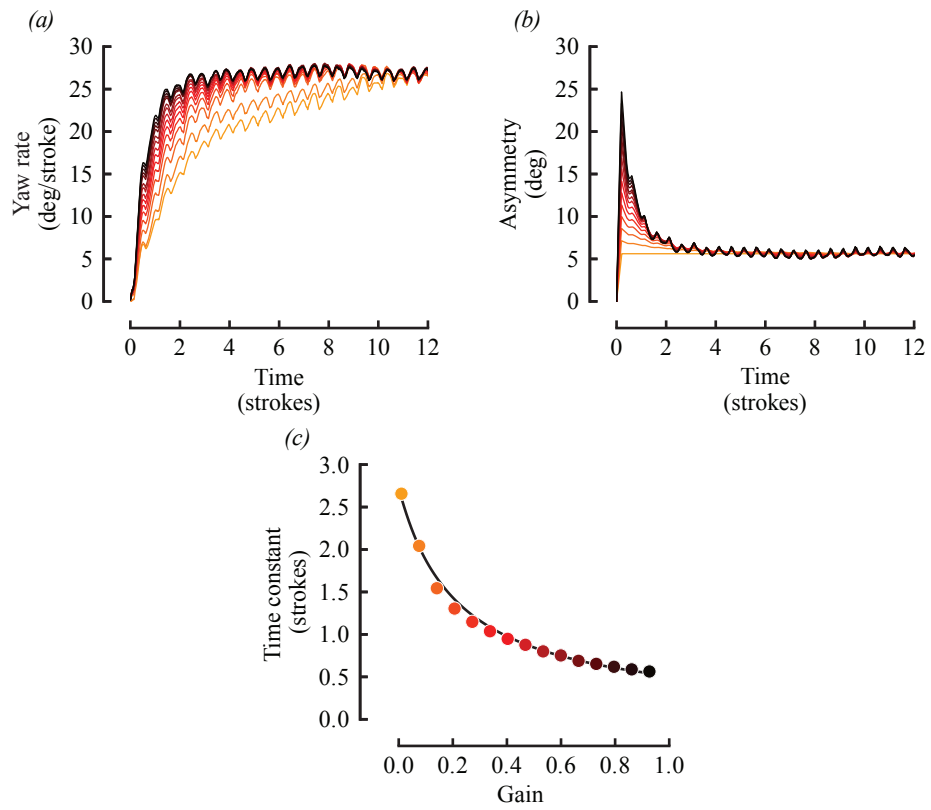
Figure 2.5: Step responses in yaw rate for a proportional controller in the absence of sensor delay for a variety of gain values. Color corresponds to gain across all panels. Time series data of the yaw velocity response *(a)* and the asymmetry parameter, *u (b)*, from the robotic model. *(c)* Time constant of the step response for a given controller gain for the robot and for simulation data.

angle of attack asymmetries (Figure 2.5b) that are much larger than those observed in *Drosophila* during high-speed video sequences in free-flight (Fry et al., 2003; Bergou et al., 2009). We conducted a second set of step response experiments that were more in line with observations of real flies by imposing a 10° limit on the angle of attack asymmetry. These data are shown along with their corresponding system time constants in Figure 2.6. The morphological limit on the angle of attack asymmetry reduced the impact of controller gain, producing an asymptotic floor in the system time constant.

2.3.2 Stability in the delayed system

To examine the destabilizing effect of sensor delay we conducted impulse response experiments for four values of feedback delay, spanning the range of relevant delays expected in a fly. The four feedback delays we considered were 0.5, 1, 5, and 10 wing strokes, with the range of controller gains used for each delay chosen based on simulation results. For each delay, we measured the response to a modified impulse in u_{ff} for a series of gains to determine the gain at which the system becomes unstable. The modified impulse consisted of a positive step in u_{ff} using the same approximation for a step function as in the previous set of experiments, followed by a corresponding negative step after a duration of 4.0 wing strokes. We fit a harmonic function with a hyperbolic tangent amplitude-envelope to the yaw rate time series data following the termination of the impulse by optimizing a least squares cost function. The asymptotic nature of the amplitude was used to determine the stability of each trajectory. The time series data is shown for the 5 wing beat delay case in Figure 2.7a to illustrate the method of finding the gain value at the stability transition. The yaw rate data display a characteristic oscillatory behavior with a period that is relatively independent of gain. The amplitude of the oscillation decays to zero for stable cases and grows toward a limit cycle for the unstable cases. The trials with other delays yielded similar results with different periods of oscillation and limit cycle amplitudes. The stability transition gain is plotted in Figure 2.7b with a comparison to model
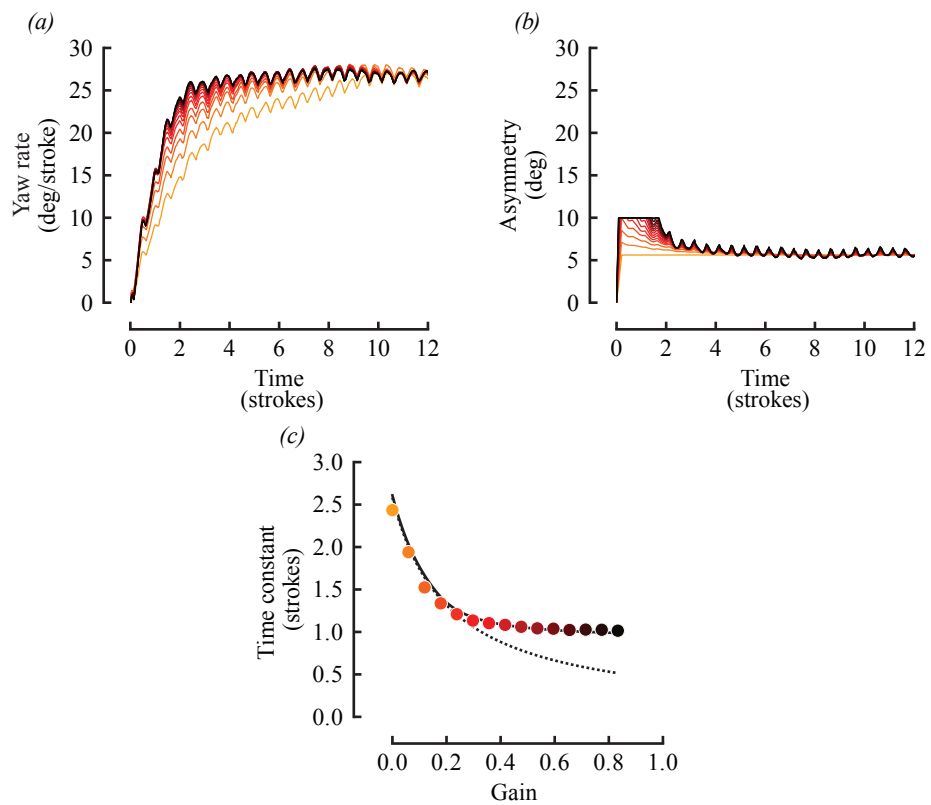
Figure 2.6: Step responses in yaw rate for a proportional controller in the absence of sensor delay with a morphological limit on the magnitude of the wing rotation angle asymmetry for a variety of gain values. Color corresponds to gain across all panels. Time series data of the yaw velocity response *(a)* and the asymmetry parameter, u *(b)*, from the robotic model. *(c)* Time constant of the step response for a given controller gain for the robot and for simulation data.
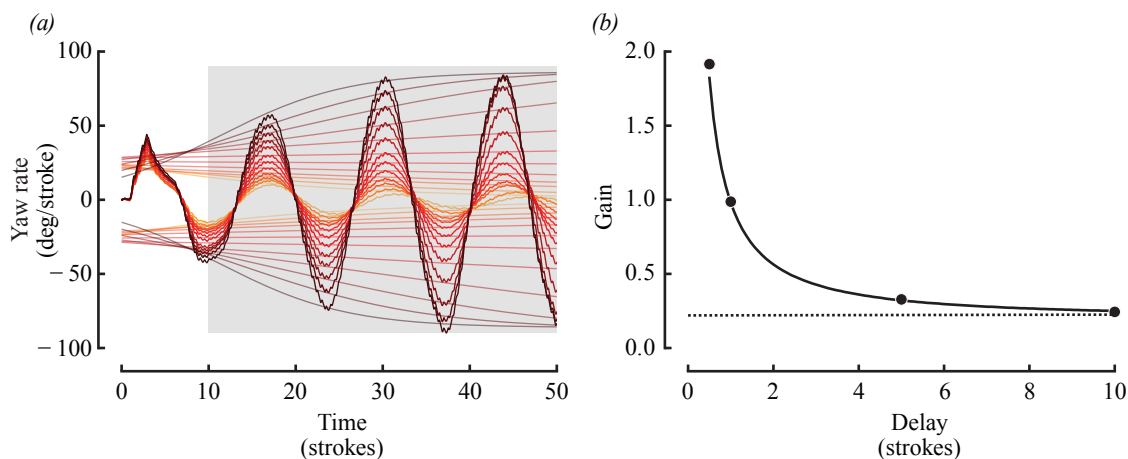
Figure 2.7: Response in yaw rate for a proportional controller with sensor delay to a modified impulse for a series of gains near the stability transition. (a) Time series yaw rate data from the robotic model for the 5 wing stroke delay case. The curves are colored in relation to the gain of the controller with higher gains corresponding to darker colors. Corresponding amplitude envelopes computed using a least squares fit over the analysis region (grey) are also plotted. (b) Stability transition gain for the robot for four delays of interest (markers) and for the stroke-averaged simulation model. The stability threshold given by Equation 2.18 is shown as a dashed line.

predictions. The results indicate a fundamental tradeoff in permissible gain and delay for gains above a certain threshold. For gains below this threshold, the system appears to be stable regardless of delay.

2.3.3   Step responses in the delayed system

Even at gains below the stability curve, sensor delay can have detrimental effects on system performance. Following the same protocol as used in the step response experiments for the undelayed system, we conducted trials with the same four feedback delays of interest as the impulse response trials. The range of controller gains used for each delay spanned the neighborhood of a critically damped response. The gain

values were once again chosen based on simulation results. With sufficient feedback gain, sensor delay introduces ringing in the step responses which is characteristic of systems of second order and higher (see Figure 2.8a). Percent overshoot of the steady-state yaw velocity was used as a performance metric and is plotted against controller gain in Figure 2.8b for the 1 wing stroke delay case. The 5% overshoot gain was estimated by spline interpolation of the overshoot curve and is shown as a function of delay and compared to simulation results in Figure 2.8c. The gain-delay curve exhibits a similar tradeoff as in the stability case, but without a gain threshold. For large enough delay, the system appears underdamped even for an arbitrarily small gain.

The data deviated noticeably from the stroke-averaged model predictions during the initial overshoot. We attributed this discrepancy to the oscillation in yaw velocity at wing beat frequency that was superimposed on the largely second order step response. The phase relationship of the wing beat frequency oscillation with the time of the peak in the step response could cause a systematic overestimate or underestimate, because phenomena within an individual stroke obviously cannot be resolved in a stroke-averaged simulation. As a check of this hypothesis, we adjusted the phase of the step change in the asymmetry parameter relative to the wing beat cycle to show this could account for the observed variation and the dominant dynamics remained unchanged.

2.4   Discussion

The results of this study highlight the importance of explicitly addressing the impact of delay when modeling the flight control system in *Drosophila* and other insects. Despite the open-loop yaw velocity dynamics being passively stable (Hedrick et al., 2009; Dickson et al., 2010; Hesselberg and Lehmann, 2007; Cheng et al., 2010), time delays consistent with those present in a fly's nervous system are sufficient to destabilize the closed-loop system for high enough gain. This system instability was observed even when only subjected to inherent process noise and not given a commanded input, u_{ff}
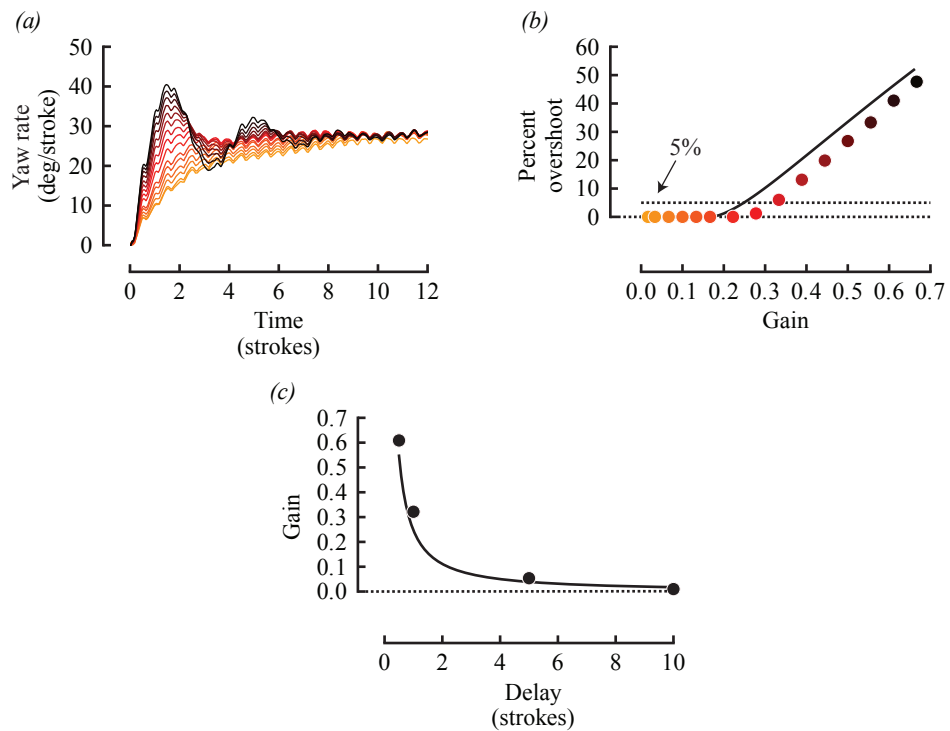
Figure 2.8: Step response characteristics for a proportional yaw rate controller with sensor delay for a series of gains near the critically damped condition. *(a)* Time series yaw rate data from the robotic model for the 1 wing stroke delay case. The curves are colored in relation to the gain of the controller with higher gains corresponding to darker colors. *(b)* Percent overshoot as a function of gain for the robotic model (red markers) and for the stroke-averaged simulation (black). *(c)* 5% overshoot gain for the robot for four delays of interest (markers) and for the stroke-averaged simulation model.

(see Figure 2.9). Introducing proportional control reduces the system time constant by adding an active damping component (Figure 2.5). For the undelayed case, this effect is limited only by the saturation of the actuation torque and any morphological limit on the asymmetry in angle of attack. For delayed feedback, the length of delay places fundamental limits on the controller bandwidth and likewise on the permissible gain. Measured responses to a modified impulse function provided a consistent means of identifying the region of gain-delay space in which the system is stable. In addition, these experiments revealed an asymptote in the gain-delay curve that provides a threshold below which the system is stable regardless of delay. However, even if the system is stable, additional delay can accrue important performance deficits. Step responses in the delayed system with sufficiently high gain displayed undesirably large amounts of overshoot and ringing, indicative of severely underdamped systems of second-order or higher. For longer delays, this behavior was unavoidable even with minimal feedback gain.

2.4.1 Active damping

Recent studies have suggested that the angular deceleration phase of yaw turns in flying animals is entirely mediated by passive damping (Hedrick et al., 2009). The authors make the argument for passive deceleration based on a comparison of published data to two separate hypotheses: a passively damped model and an active model whereby asymmetric flapping generates constant braking torque. The passive model predicts an exponential decay in yaw rate, similar to real trajectories, whereas the active constant torque model predicts a linear decay. Dynamically-scaled robotic experiments and computational methods have shown that aerodynamic damping in flapping flight is indeed important to the dynamics of yaw turns (Dickson et al., 2010; Cheng et al., 2010; Hesselberg and Lehmann, 2007). In addition, these studies showed that the resulting passive dynamics are approximately first-order and linear in rotation rate, which would lead to the observed exponential decay. However, the existence of strong compensatory reflexes in flies that depend on the magnitude of
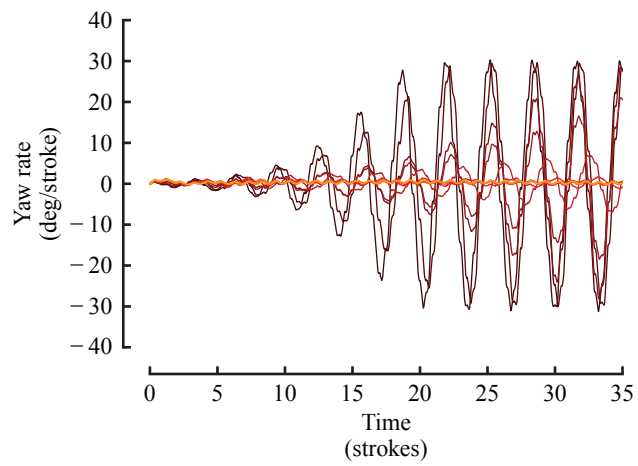
Figure 2.9: Response in yaw rate to inherent process noise for a proportional controller with sensor delay for a series of gains near the stability transition. Time series yaw rate data are shown from the robotic model for the 1 wing stroke delay case. The curves are colored in relation to the gain of the controller with higher gains corresponding to darker colors.

the stimulus would suggest that these insects utilize active stabilization that may be approximated by proportional feedback (Frye and Gray, 2005; Taylor and Krapp, 2008). As is evident from the time series step response data, as well as an analysis of the stroke-averaged equations, a proportional feedback controller would also exhibit exponential decay. Thus, the existence of an exponential decay in yaw rate cannot be taken as evidence for the absence of active feedback. Consider the transfer function for the closed loop dynamics of the linear stroke-averaged model under proportional control, $G(s)$:

$$G(s) = \frac{k_p C_u}{Is + C_\omega + k_p C_u} = \frac{k_p C_u}{Is + \hat{C}_\omega}. \tag{2.14}$$

The characteristic equation for the closed loop system has the same form as the process dynamics with an effective damping of $\hat{C}_\omega = C_\omega + k_p C_u$. In a stroke-averaged sense, proportional feedback decreases the time constant of the system by providing an active form of damping.

Flies, like most animals, use a combination of feedforward motor programs and both neural and mechanical feedback during locomotion (Dickinson et al., 2000). Given the relatively short time course associated with saccades, there is some question as to whether or not the feedback component is involved at all during such maneuvers (Bender and Dickinson, 2006a). *Drosophila* exhibit strong visual- and haltere-mediated equilibrium reflexes to rotational stimuli (Dickinson, 1999; Ristroph et al., 2010; Götz, 1968, 1975), providing some evidence for respective feedback circuits. However, such reflexes could be suppressed during voluntary maneuvers. Previous research on magnetically-tethered *Drosophila*, where the animal is allowed one degree of freedom about the yaw axis, has suggested mechanosensory feedback from the haltere influences a feedforward motor program in determining saccade dynamics whereas visual feedback plays little or no role subsequent to the initiation (Bender and Dickinson, 2006a). Researchers conducting free flight studies of mechanically induced yaw perturbations concluded the feedback signal from the haltere was used to generate reflexive course corrections, but the animals did not use active braking dur-

ing the perturbation nor at the termination of the compensatory maneuver (Ristroph et al., 2010). In light of the potential implications of sensory delay on an actively controlled deceleration, it may even seem prudent for animals to perform these fast maneuvers in open-loop. However, feedback systems are ubiquitous across biological systems and engineering applications alike, presumably because they provide robustness to uncertainty. Whereas the term robustness has very specific connotations in control systems, anecdotal observations of fruit flies convey the general concept of their ability to handle external perturbations, uncertain process dynamics, and internal asymmetries. Drosophila are able to regulate yaw torque with partial wing ablations, artificially added wing mass, and many other manipulations (Bender and Dickinson, 2006a). Further, the moment of inertia of a fruit fly may vary greatly not only over their lifetime, but even during the course of the day given its hunger state or gravidity. Such observations do not necessarily lead to any direct conclusions about the role of feedback during rapid maneuvers, but the universal nature of feedback in these systems invites consideration of it at all timescales. We will attempt to construct a simple feedback model of the visual and haltere systems that is consistent with observations in behavioral studies of yaw dynamics and incorporates the influence of sensor delay.

2.4.2 Active damping for delayed feedback

Proportional feedback with finite sensor delay also provides active damping, with the caveat that only sufficiently long timescales and sufficiently low gains are considered. Using a first order Pade approximation for delay yields the closed-loop transfer function (Aström and Murray, 2010),

$$G_\delta(s) = \frac{k_p C_u(2 + s\delta)}{2(C_\omega + k_p C_u + Is) + s(C_\omega - k_p C_u + Is)\delta}, \tag{2.15}$$

providing valuable insight into the effect this delay has on the stroke-averaged dynamics. Such an approximation requires exercising some caution because it is valid only at low frequencies relative to the inverse of the delay time. Higher order Pade

approximations may be used to similar effect with more precision, but at the cost of sensitivity to perturbations and loss of illustrative clarity. Solving for the pole locations of $G_\delta(s)$, Equation 2.15, gives analytical expressions for the stable and critical gains, which demonstrate the tradeoff between gain and delay. Requiring the discriminant of the characteristic equation to be zero provides the condition for critical damping:

$$k_{critical} = \frac{6I + C_\omega\delta - 4\sqrt{I(2I + C_\omega\delta)}}{C_u\delta},$$ (2.16)

Requiring the poles to reside in the left half plane yields the condition for stability:

$$k_{stable} \le \frac{2I + C_\omega\delta}{C_u\delta}.$$ (2.17)

Equations 2.16 and 2.17 provide reasonable approximations of the experimentally determined gain-delay curves. In the limiting case of zero delay, all timescales are long relative to the delay, allowable gain goes to infinity, and we recover the undelayed closed-loop dynamics. Examining Equation 2.17 reveals the source of the stability threshold in gain, leading to a sufficient condition for stability:

$$k_p \le \frac{C_\omega}{C_u}.$$ (2.18)

The same asymptote appears to exist for critical damping, contrary to the experimental results. However, this is an artifact from the breakdown in our approximation for delay at long delays relative to the dynamics. To show that Equation 2.18 is still relevant for the stable gain case, we consider the loop transfer function, $L(s)$, with the full expression for delay:

$$L(s) = \frac{k_p C_u e^{-s\delta}}{Is + C_\omega}.$$ (2.19)

We assess the stability of the closed-loop system by applying the Nyquist criterion. With the condition on k_p given by Equation 2.18, the H-infinity norm is less than one, which guarantees stability but is not particularly useful for most performance

metrics. The stability threshold in gain, therefore, results from the strength of passive damping relative to disturbances from a delayed control input.

On sufficiently long timescales relative to the delay, Equations 2.15-2.18 provide a valid description of the dynamics and we may use them to compute an effective damping similar to the undelayed case. The relevant term is the real part of complex conjugate poles in $G_\delta(s)$, Equation 2.15, which gives the decay rate. Normalizing by the moment of inertia gives the effective damping:

$$\hat{C}_\omega = \frac{2I + (C_\omega - k_p C_u)\delta}{2\delta},$$
$$(2.20)$$

which is relevant for gains near $k_{critical}$. Shorter delay allows for larger effective damping and a faster system response.

2.4.3   Performance limits

Time delays impose fundamental limits on the performance of the closed-loop system which may be analyzed using the crossover frequency inequality (Aström and Murray, 2010):

$$-\arg P_{ap}(i\omega_{gc}) \le \pi - \phi_m + \frac{n_{gc}\pi}{2} = \phi_l,$$
$$(2.21)$$

where $P_{ap}(s)$ is the all pass system containing the non-minimum phase portion of the loop transfer function; ω_{gc} is the gain cross-over frequency; ϕ_m is the desired phase margin; n_{gc} is the slope of the gain curve at cross-over; and ϕ_l is admissible phase lag in the minimum phase component of the dynamics. Decomposing Equation 2.19 and applying Equation 2.21 we get the following condition on ω_{gc}:

$$\omega_{gc} \le \frac{\phi_l}{\delta},$$
$$(2.22)$$

meaning that time delay limits the maximum permissible cross-over frequency and longer time delays impose more restrictive conditions. This results in an expression for gain for a desired level of phase margin, k_{ϕ_m}:

$$k_{\phi_m} = \sqrt{\frac{(\pi - \phi_m + \frac{n_{gc}\pi}{2})^2 I^2 + C_\omega^2 \delta^2}{C_u^2 \delta^2}}. \tag{2.23}$$

A large cross-over frequency is desirable both for controller tracking and load disturbance rejection at higher bandwidth and is facilitated by high gain. Longer delay with the same amount of phase margin demands a lower cross-over frequency. Delay, therefore, dictates the nature of the tradeoff between robustness and response time.

2.4.4 Visual and mechanosensory feedback integration

There is strong anatomical and physiological evidence that suggest the primary flight control sensors for detecting yaw rate in flies, namely the vision system and the halteres, have evolved under selective pressure to reduce latency (Braitenberg, 1967; Trimarchi and Murphey, 1997; Fayyazuddin and Dickinson, 1996). This idea is consistent with the tangible fitness associated with performance limits imposed by sensory delays. The specializations in flies' sensory systems may facilitate their high performance behavior (Parsons et al., 2010). Tethered-flight experiments offer a method to decouple and systematically measure visual and mechanical gain, but have often been criticized for producing exaggerated responses compared to similar disturbances in free-flight (Taylor et al., 2008). We will look at the open loop responses to visual and mechanical yaw velocity stimuli in the context of our results and provide a potential reconciliation of the observed open-loop responses with free-flight yaw dynamics.

Previous studies of tethered *Drosophila* measured bilateral difference in wing beat amplitude (ΔWBA) tuning curves independently for visual and mechanical yaw velocity stimuli (Sherman and Dickinson, 2003). Using a calibration of ΔWBA to yaw torque of $9.36 \times 10^{-9} \text{NmV}^{-1}$, estimated from data in another study using the same wing beat analyzer instrument (Tammero et al., 2004), we obtain a crude estimate for haltere and visual feedback gain. Direct torque measurements in response to visual stimuli performed in an earlier study provides some independent confirmation of this estimate (Blondeau and Heisenberg, 1982). For mechanical stimuli, yaw torque
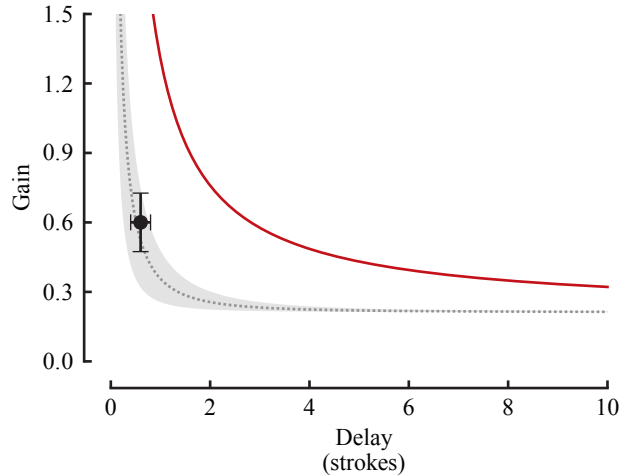
Figure 2.10: Estimated feedback gain and delay properties for *Drosophila* in relation to theoretical stability and performance boundaries for proportional feedback from the haltere. Data point (black) is estimated from published data (Sherman and Dickinson, 2003; Tammero et al., 2004). Theoretical stability curve is shown in solid red and the $60° \pm 15°$ phase margin region computed from Equation 2.23 is shaded in gray.

was approximately linear with yaw rate, with a slope consistent with a proportional controller of $k_p = k_{haltere} = 0.6$. This estimate of gain comes from the nondimensionalized slope of regressed mechanical response data (Sherman and Dickinson, 2003), multiplied by the torque calibration constant and normalized by C_u. Given the estimated feedback delay of the haltere, this gain is in close agreement with what would be expected for a proportional controller conforming to traditional control systems design criteria. The estimated haltere-based controller falls between the $75°$ and $45°$ phase margin lines, given by Equation 2.23, on our gain-delay plot in Figure 2.10.

With the longer delay associated with the visual system, one might expect the gain to be much smaller in the visual system. However, over the region where the visual response is proportional to the stimulus, the gain is actually much larger with $k_p = k_{visual} = 12.2$, which would be remarkably unstable according to our results.

The important features of the visual response that this neglects is the roll-off that occurs at roughly $\omega_c = 0.7\,\mathrm{Hz}$ and the influence of haltere feedback on the dynamics. A better interpretation of a visually-mediated yaw controller is a low-pass filter. We estimate the controller transfer function to be:

$$C_{visual} = \frac{k_{visual}\omega_c}{s + \omega_c}. \tag{2.24}$$

For short delays, such as a feedback loop from the halteres, the permissible cross-over frequency is larger than the process pole, meaning that large steady-state gain and small tracking error over low frequencies can be achieved with a simple proportional controller. For the visual system, the permissible cross-over frequency is smaller than the process pole, which in this case necessitates the addition of a low frequency pole. A low pass filter provides the most basic implementation of this requirement. If we consider the controller in Equation 2.24 applied to the passive dynamics, the steady-state gain is too high and the resulting system is still unstable (See Figure 2.11). However, the haltere delay is small on the timescale of the visual system and proportional feedback from the haltere would provide active damping. The plant dynamics to consider for the visual system would have an effective damping computed from the estimated haltere gain and delay using Equation 2.20. The resulting system is stabilized and has good performance characteristics.

Fast, unstable process poles require a higher cross-over frequency to control them. Since the permissible cross-over frequency for the visual system is smaller than the process pole, the process dynamics are required to be stable. The passive dynamics in yaw velocity are already stable. Added effective damping from a haltere inner feedback loop is, therefore, not necessary for stability, but does allow the visual system to operate at higher gain with faster response for the same level of robustness. It is conceivable that flies could have visually controlled stable yaw dynamics in the absence of halteres with either larger passive damping or lower visual gain. Hind wings would presumably provide larger passive damping, whereas low latency rate sensors provided by halteres would allow for a larger amount of active damping. The conser-
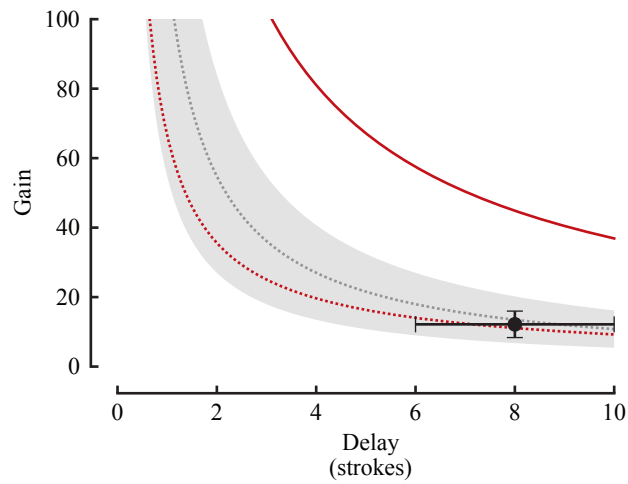
Figure 2.11: Estimated feedback gain and delay properties for *Drosophila* in relation to theoretical stability and performance boundaries for proportional feedback from a visual feedback low-pass filter with inner-loop haltere-mediated effective damping. Data point (black) is estimated from published data (Sherman and Dickinson, 2003; Tammero et al., 2004). Theoretical stability curve is shown in solid red and the $60° \pm 15°$ phase margin region computed from Equation 2.23 is shaded in gray. The dashed red line gives the stability curve for the visual feedback without active damping.

vation of overall damping characteristics may very well have paved the way for the evolution of the haltere from the hind wing. A yaw rate stabilization reflex consisting of an inner-loop proportional controller from haltere feedback that provides effective damping for an outer-loop visual low-pass filter is consistent with open-loop measurements in tethered flight and provides performance and robustness characteristics expected by engineering design principles. In addition, the low cut-off frequency of the visual system, which is necessarily low due to the permissible cross-over frequency resulting from the visual system delay, explains why visual responses during saccades and other fast maneuvers are not prominent. A block diagram illustrating the control architecture is shown in Figure 2.12. This provides some evidence that tethered flight responses might not be exaggerated, but are indeed what would be expected of an open-loop response for a well-tuned flight control system in contradiction to previous arguments (Taylor et al., 2008). Flies possess delay tolerant passive flight dynamics and have additionally combated the effects of sensor delay through the evolution of latency reducing specializations. Yet, because of absolute limits posed by neurobiological constraints, sensor delay remains a pervasive influence on flight dynamics and constant limitation on flight performance. These results lend themselves to applications in micro-air vehicle design as well as in developing a better understanding insect flight control strategies.
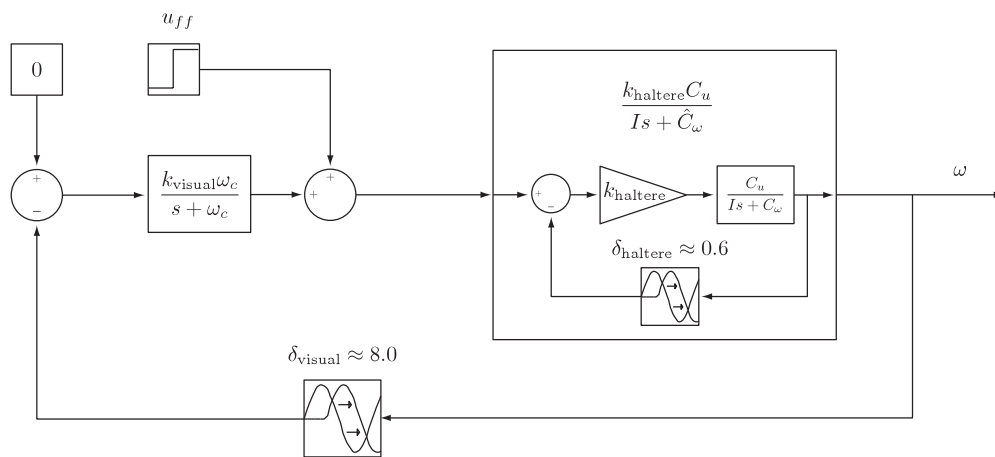
Figure 2.12: Block diagram of proposed yaw rate control architecture in *Drosophila*, given estimated feedback gain and delay properties for a visual feedback low-pass filter with inner-loop haltere-mediated active damping.

Chapter 3

Wing kinematics and the stabilization of longitudinal forward flight

Flying insects perform impressive flight maneuvers that remain unmatched by micro-robotic systems.

—Chauncey Graetzel (2010)

3.1 Summary

The ability to regulate forward speed is an essential requirement for flying animals. Here, we use a dynamically-scaled robot to gain insight into how flapping insects adjust stroke features to regulate and stabilize level forward flight. The results suggest that few changes to hovering kinematics are actually required to meet steady-state lift and thrust requirements at different flight speeds, and the primary driver of equilibrium velocity is the aerodynamic pitch moment. This finding is consistent with prior hypotheses and observations regarding the relationship between body pitch and flight speed in fruit flies. The results suggest that a shift in the mean stroke position of the flapping wings is a likely candidate for trimming the pitch moment at all speeds, whereas changes in the wing rotation angle are required only at high speeds. The results also show that the dynamics may be stabilized with the addition of a pitch damper, but that the magnitude of required damping increases with flight speed. We posit that differences in stroke deviation between the upstroke and downstroke might

play a critical role in this stabilization. Fast mechanosensory feedback of the pitch rate could enable active damping, which would inherently exhibit gain scheduling with flight speed if pitch torque is regulated by adjusting stroke deviation. Such a control scheme would provide an elegant solution for flight stabilization across a wide range of flight speeds.

3.2   Materials and methods

3.2.1   Robotic fly apparatus

We conducted the experiments in a 1m × 2.4m × 1.2m tank of mineral oil (Cheveron Superla white oil; Chevron Texaco Corp. San Ramon CA, USA; density 880 kg/m3, kinematic viscosity 115 cSt at 25°C) using a dynamically-scaled model of *Drosophila* with similar hardware to the apparatus described previously (Dickson et al., 2010; Elzinga et al., 2012). The robot consists of two isometrically scaled acrylic wings (length (R) = 230 mm, mean chord ($\bar{c}$) = 65 mm, width = 2.3 mm), each with three independently actuated degrees of freedom: stroke angle (ϕ), deviation angle (θ), and rotation angle (α), as illustrated in Figure 3.1*(b)* and following a standard Euler angle convention for wing kinematics (Lehmann and Dickinson, 1997). The stroke axes of the two wings were parallel and separated by 0.11 m. The stroke position of each wing was controlled by a stepper motor using a microstepping driver (M-1715-1.5D, IM483; Schneider Electric Motion, Marlborough, CT, USA) whereas the rotation and deviation positions were controlled by digital servo motors (HSC-5996TG, Hitec RCD, Poway, CA, USA). The wing motor assemblies were attached to a common base plate. A 6-axis silicon strain-gauge-based transducer (Nano-43, ATI, Apex, NC, USA) coupled the base plate with the pitch rotation stage and measured forces and moments in the body frame, which were then transformed in software to the center-of-mass coordinate system shown in Figure 3.1*(c)*. The pitch rotation of the airframe was actuated by a stepper motor (M-2218-3.0S, IM483; Schneider Electric Motion, Marlborough, CT, USA). The location of the pitch axis was adjusted
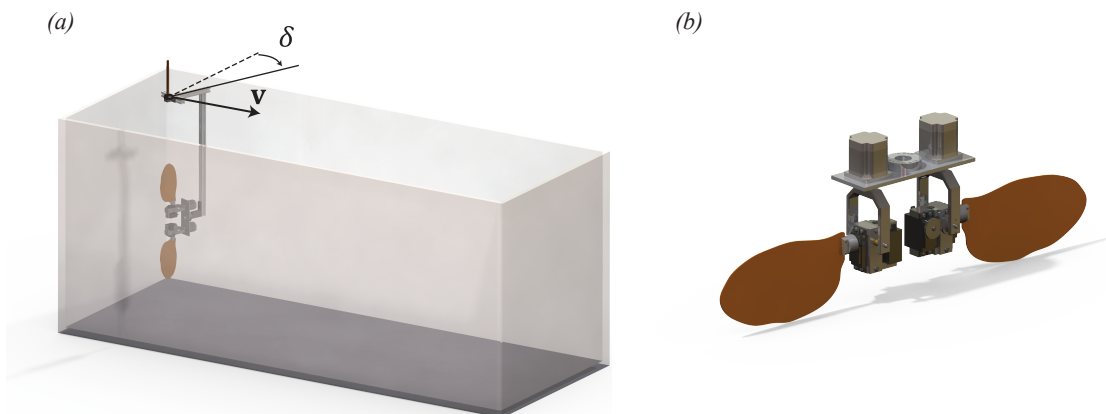
Figure 3.1: Experimental apparatus. *(a)* Design drawing of the dynamically scaled robotic model immersed in the mineral oil tow tank with a *(b)* detail view of the wing motor assemblies. Each wing has three degrees of freedom, stroke (ϕ), deviation (δ), and rotation (α). Forces and torques are measured where the base fixture that joins the two wing motor assemblies meets the pitch rotation yoke.

relative to the hinge location to coincide with the center-of-mass of the virtual body. A geometrically scaled body model was not used because the influence of the interaction between the body and wings on the aerodynamic forces is relatively small and can be ignored for most studies (Hesselberg and Lehmann, 2007; Dickson et al., 2010; Hedrick et al., 2009). The entire apparatus was mounted on a linear translation stage comprised of two linear rails driven by timing belts (Custom, Thomson Industries, Inc., Radford, VA, USA), which were actuated with a single brushless servo-motor (BM200E, Aerotech, Inc., Pittsburgh, PA, USA) (Figure 3.1*(a)*).

The robot was controlled using a PC running a hard real-time Linux kernel with custom software written in Python and C. At each time step within a 3 kHz real-time loop, forces and torques were measured, and the commanded positions for all of the actuators were updated based on prescribed wing and body kinematics. To achieve appropriate dynamic scaling of the wing and body motions, we matched the Reynolds
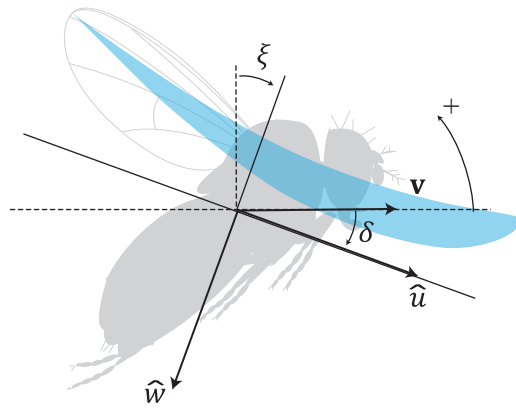
Figure 3.2: Body-fixed, center-of-mass coordinate system used in defining the equations of motion, Equation 3.21, where the pitch angle (ξ) is measured relative to the stroke plane at hover (defined as horizontal in the lab frame with the long axis of the body pitched up at 62° relative to the stroke plane). δ is the body pitch angle relative to the velocity vector, which is equivalent to ξ only in level forward flight. The positive direction is shown for axis tangential (normal) to the stroke plane, u (w). For ξ and δ, counter-clockwise is positive.

number (Re), dimensionless pitch velocity (ω^*), and the advance ratio (J) of the robot to that of a fruit fly with a wing beat frequency of 200 Hz and mean wing chord ($\bar{c}$) of 0.76 mm. These dimensionless quantities are defined by the following:

$$\text{Re} = \frac{2R\Phi f\bar{c}}{\nu}, \tag{3.1}$$

$$\omega^* = \frac{\omega}{f}, \tag{3.2}$$

$$J = \frac{V}{2R\Phi f}, \tag{3.3}$$

where R is the wing length, Φ is the (peak-to-peak) stroke amplitude, f is the flapping frequency, ν is the kinematic viscosity, ω is the angular velocity of the body, and V is the velocity of the body. A robot flapping frequency of 0.179 Hz was used to yield a Re of 114, consistent with flapping flight in *Drosophila* (Lehmann & Dickinson 1997). The forces (F) and torques (τ) measured by the robot were nondimensionalized according to Equations 3.4 and3.5 (Fry et al. 2003; Dickson et al. 2010):

$$F^* = \frac{F}{\rho f^2 \bar{c}^4}, \tag{3.4}$$

$$\tau^* = \frac{\tau}{\rho f^2 \bar{c}^5}, \tag{3.5}$$

where ρ is the fluid density. The dimensionless forms of the remainder of terms to appear in the dynamics are given in Equations 3.6 and 3.9:

$$m^* = \frac{m}{\rho \bar{c}^3}, \tag{3.6}$$

$$I^* = \frac{I}{\rho \bar{c}^5}, \tag{3.7}$$

$$a^* = \frac{a}{f^2 \bar{c}}, \tag{3.8}$$

$$V^* = \frac{V}{f\bar{c}}, \tag{3.9}$$

where m is the mass, I is the moment of inertia, a is the linear acceleration, and the asterisk indicates the corresponding dimensionless quantity. The dimensionless mass (m^*) and moment of inertia (I^*) about the pitch axis used in this study were 1.93×10^3 and 1.74×10^3, respectively, in agreement with those used in previous studies (Cheng and Deng, 2011). This was calculated by modeling the fly as a cylinder with length of 2.5 mm and mass of 1.0 mg. All subsequent values and equations will appear in their appropriate dimensionless form as defined by Equations 3.1 and 3.9 with the asterisk notation dropped unless noted explicitly otherwise.

3.2.2 Wing kinematics

We used idealized Drosophila wing kinematics consisting of a nominal set of hovering kinematics based on previous work (Berman and Wang, 2007), augmented with several biologically plausible deformation modes which we have found, through quasi-steady simulations, to generate pitch torque. The stroke position, deviation, and rotation angle for the baseline kinematics are given as follows:

$$\phi_b(t) = \frac{\phi_0}{\arcsin(k_\phi)} \arcsin[k_\phi \cos(2\pi f t)], \tag{3.10}$$

$$\theta_b(t) = 0, \tag{3.11}$$

$$\alpha_b(t) = \frac{\alpha_0}{\tanh(k_\alpha)} \tanh[k_\alpha \sin(2\pi f t)], \tag{3.12}$$

where ϕ_0 is the stroke amplitude, α_0 the rotation amplitude, and the parameters k_ϕ and k_α control the shape of the wing kinematics. Values of $k_\phi = 0.01$ and $k_\alpha = 1.5$

were selected to produce waveforms that resemble an idealized version of the wing kinematics of *Drosophila* (Berman and Wang, 2007; Dickson et al., 2010). Similarly, a value of $\phi_0 = 70°$ was used to give a peak-to-peak stroke amplitude of 140° and a value of $\alpha_0 = 45°$ was used to give a 45° angle of attack at mid-stroke under hovering conditions.

We considered three different deformations of hovering wing kinematics: a shift in the mean stroke position (mean stroke offset mode), upstroke to downstroke differences in wing rotation angle (wing rotation offset mode), and upstroke to downstroke differences in stroke deviation (differential deviation mode). The shift in mean stroke position is accomplished by adding the deformation parameter to the stroke position, Equation 3.10, yielding Equation 3.13,

$$\phi(t) = \phi_b(t) + u_{ms}, \tag{3.13}$$

where u_{ms} is the deformation parameter. A positive u_{ms} shifts the mean stroke position, and likewise the mean center of pressure, anterior to the center-of-mass, generating a positive pitch torque. An example trace of the wing kinematics illustrating a nonzero value for u_{ms} is shown in Figure *3.9(a)*.

The wing rotation mode shifts the baseline rotation angles in the following manner, leaving the other degrees of freedom unchanged:

$$\alpha(t) = \alpha_b(t) + u_{wr}, \tag{3.14}$$

where u_{wr} is the deformation parameter. A positive u_{wr} lowers the angle of attack on the upstroke, reducing drag while having the opposite effect on the downstroke. Because the mean center of pressure is above the center-of-mass, this results in a positive pitch torque. An example trace of the wing kinematics illustrating a nonzero value for u_{wr} is shown in Figure 3.9*(a)*.

Differences between upstroke and downstroke deviation were modeled as sinusoidal excursions from the stroke plane at wing beat frequency over each half stroke with the maximum deviation occurring at mid-stroke. The differential deviation mode is

described by Equation 3.15:

$$\theta(t) = -\frac{1}{2}u_{dd}\sin(2\pi ft)(1 + \text{sgn}[u_{dd}\sin(2\pi ft)]), \qquad (3.15)$$

where u_{dd} is the deformation parameter. Positive (negative) values of u_{dd} contribute to a ventral deviation only on the upstroke (downstroke), reducing the mean moment arm over the upstroke (downstroke) for the drag component of forces on the wings, resulting in a net positive (negative) stroke-averaged pitch torque. An example trace of the wing kinematics illustrating a nonzero value for u_{dd} is shown in Figure *3.9(a)*.

3.2.3 Aerodynamic force and moment measurements

Using the dynamically-scaled robotic fly apparatus, we measured the forces and moments generated during longitudinal flight as a function of the state, $\mathbf{x}$, and the kinematic deformation, $\mathbf{u}$, as defined by Equations 3.16-3.20:

$$\mathbf{x} = \begin{bmatrix} v_u \\ v_w \\ \omega \\ \xi \end{bmatrix}, \qquad (3.16)$$

$$\delta = \arctan(\frac{v_w}{v_u}), \qquad (3.17)$$

$$s = \sqrt{v_u^2 + v_w^2}, \qquad (3.18)$$

$$\mathbf{v} = \begin{bmatrix} v_u \\ v_w \end{bmatrix}, \qquad (3.19)$$

$$\mathbf{u} = \begin{bmatrix} u_{ms} \\ u_{wr} \\ u_{dd} \end{bmatrix}, \qquad (3.20)$$

	u_{ms}	u_{wr}	u_{dd}
minimum	$-22.2°$	$-20.0°$	$-20.0°$
maximum	$18.8°$	$20.0°$	$20.0°$

Table 3.1: Range of kinematic deformation parameter values used in force and moment measurements

where v_u is the body velocity tangential to the stroke plane, v_w is the body velocity normal to the stroke plane, ω and ξ are body pitch rate and body pitch, respectively, relative to an inertial reference frame, s is the flight speed (the Euclidean norm of $\mathbf{v}$), and δ is a convenience variable describing the slip angle (see Figure 3.2). The experiments we conducted to systematically examine the parameter space were composed of three general types: a variation of the kinematic deformation parameters while the robot was stationary, pitch rotations at constant rotation rate for a fixed set of wing kinematics at zero translational velocity, and constant velocity translations at a constant body pitch relative to the velocity vector for a fixed set of wing kinematics. First, we performed the kinematic deformation mode experiments to measure $g_n(\mathbf{u})$, $g_t(\mathbf{u})$, and $N(\mathbf{u})$, the baseline subtracted aerodynamic force normal to the stroke plane, tangential to the stroke plane, and the aerodynamic pitch moment respectively, all as a function of the deformation parameters (u_{ms}, u_{wr}, and u_{dd}). The effects of each of these parameters were assumed to be additive and independent, a reasonable assumption based on previous work (Dickson et al., 2010). Consequently, we did not perform experiments involving combinations of the deformation modes. Trials consisted of 6 wing strokes at 11 linearly spaced constant values of the deformation parameter for each of the three deformation modes. Based on the initial results for the mean stroke offset mode, an offset of $u_{ms} = -7.2°$ was included in all subsequent experiments, which served to trim the nominal pitch moment generated by the baseline kinematics (Equations 3.10-3.12). For each mode, the minimum and maximum values of the deformation parameter we considered spanned the range where the pitch moment was approximately linear (see Table 3.1). Stroke-averaged forces and moments were determined by averaging over the last three wing strokes of the trial.

To measure C_ω, the pitch damping coefficient, we conducted trials that consisted of 2 wing strokes with the robot stationary, followed by a step change in the pitch rotation rate, ω, that was held for 5 wing strokes. These trials were carried out for 13 linearly spaced constant values of ω over the range of -36 to $36°\text{stroke}^{-1}$. The stroke-averaged pitch torque was determined by averaging over the last three wing strokes of the trial. We computed C_ω from a least squares linear fit of the relationship between stroke-averaged pitch torque and pitch rate with the sign convention that a positive C_ω is dissipative. We measured $f_n(\delta, s)$, $f_t(\delta, s)$, and $M(\delta, s)$, the aerodynamic force normal to the stroke plane, tangential to the stroke plane, and the aerodynamic pitch moment, respectively, as functions of the slip angle and velocity magnitude, by conducting constant velocity translation experiments with the robot at a constant body pitch relative to the velocity vector. The trials consisted of 5 wing strokes with the robot stationary, followed by a step change in forward velocity that was held for 3 wing strokes. Longer flight bouts were not possible because the robot traversed the entire length of the tank during the three wing strokes when operating at the top of the speed range. The velocities used in this study spanned a range of 0.1 to 1ms^{-1} in increments of 0.1ms^{-1} (The 0.0ms^{-1} case was accounted for in the deformation mode experiments) when scaled for a fruit fly. The body pitch angle was rotated relative to the forward velocity vector and the set of experiments was repeated in 5° increments over the full 360° range of relative angles for a total of 720 trials for each set of wing kinematics considered. Stroke-averaged forces and torques were taken from the last wing stroke of the trial. Example time series force and moment data for a single wing stroke over a range of flight speeds with $\delta = -15°$ and the corresponding stroke-averaged values are shown in Figure *3.3(a)* and *(b)*.

3.2.4   Stroke-averaged modeling

The stroke-averaged longitudinal dynamics in the body frame are derived from the Newton-Euler equation Murray et al. (1994) and are given by:
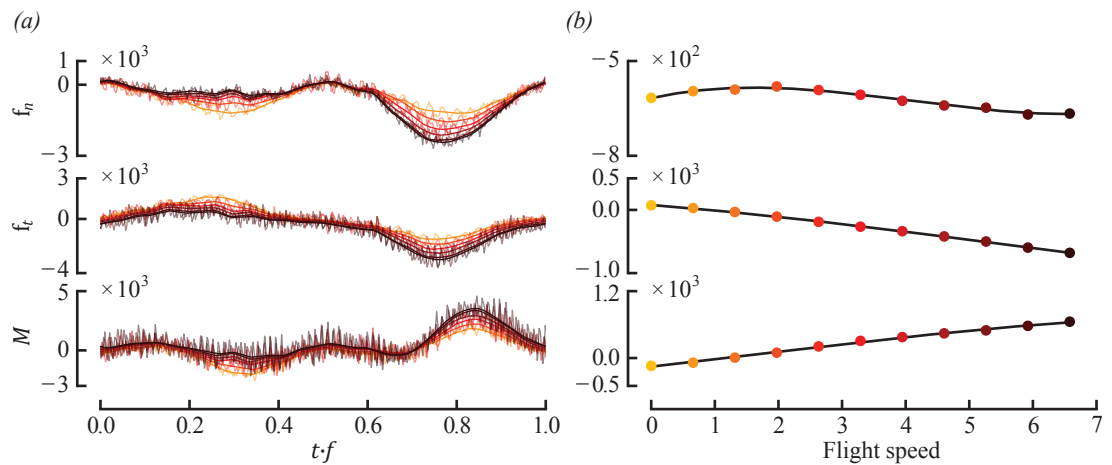
Figure 3.3: Force and moment data with $\delta = -15°$ over a range of flight speeds. *(a)* Time series force and moment data for single a wing stroke with time specified in strokes $(t \cdot f)$. Both raw and filtered traces (4th order Butterworth, zero phase delay filter) are shown and are color coordinated by flight speed with the corresponding stroke-averaged values shown in *(b)*. Filtered traces are shown for illustrative purposes only as the stroke averaged values are computed directly from the raw force and moment measurements.

$$\dot{\mathbf{x}} = h(\mathbf{x}, \mathbf{u}) = \begin{bmatrix} \frac{1}{m}(\mathrm{f}_t(\delta, s) + \mathrm{g}_t(\mathbf{u})) - \sin(\xi)g - v_w\omega \\ \frac{1}{m}(\mathrm{f}_n(\delta, s) + \mathrm{g}_n(\mathbf{u})) + \cos(\xi)g - v_u\omega \\ \frac{1}{I_{yy}}(M(\delta, s) + N(\mathbf{u}) - C_\omega\omega \\ \omega \end{bmatrix} \tag{3.21}$$

where I_{yy} is the moment of inertia about the pitch axis, and g is the acceleration due to gravity. The aerodynamic forces and moments as a function of the state, that is $\mathrm{f}_n(\delta, s)$, $\mathrm{f}_t(\delta, s)$, $M(\delta, s)$, and the term $C_\omega\omega$, were measured using the robotic fly apparatus for the baseline wing kinematics (Equations 3.10-3.12) with a constant offset in the mean stroke position that balanced the pitch moment at hover. The forces and moments that were functions of the deformation parameters ($\mathrm{g}_n(\mathbf{u})$, $\mathrm{g}_t(\mathbf{u})$, and $N(\mathbf{u})$), which serve as control inputs, were assumed not to be a function of the state, although we will explore in depth a noted and consequential exception for the differential deviation mode.

We investigated the stability of the dynamics (Equation 3.21) using custom code written in Python that utilized the SciPy module (Jones et al., 2010) by linearizing the dynamics about a series of equilibrium (denoted with subscript e) operating points, $(\mathbf{x}_e, \mathbf{u}_e)$, for level forward flight:

$$\mathbf{x}_e = \begin{bmatrix} s\cos(\delta) \\ s\sin(\delta) \\ 0 \\ \delta \end{bmatrix}, \qquad h(\mathbf{x}_e, \mathbf{u}_e) = \begin{bmatrix} 0 \\ 0 \\ 0 \\ 0 \end{bmatrix} \tag{3.22}$$

$$\dot{\mathbf{z}} = A\mathbf{z} + B\mathbf{w}, \qquad A = \left.\frac{\partial h}{\partial \mathbf{x}}\right|_{(\mathbf{x}_e, \mathbf{u}_e)}, \qquad B = \left.\frac{\partial h}{\partial \mathbf{u}}\right|_{(\mathbf{x}_e, \mathbf{u}_e)}, \tag{3.23}$$

where $\mathbf{z}$ is the state $(\mathbf{x} - \mathbf{x}_e)$, $\mathbf{w}$ is the control input $(\mathbf{u} - \mathbf{u}_e)$, A is the linearized dynamics matrix, B is linearized control matrix. Stability is determined by the real part of the eigenvalues of A, where a strictly negative real part for all four eigenvalues indicates an asymptotically stable system.

3.3   Results

3.3.1   Measurement of the stroke-averaged drift dynamics

The aerodynamic forces and moments generated during longitudinal flight as a function of the slip angle, δ, and the magnitude of translational velocity for a baseline set of hovering wing kinematics are shown in pseudo color plots in Figure 3.4. These functions, which represent $f_n(\delta, s)$, $f_t(\delta, s)$, and $M(\delta, s)$, were computed by fitting tensor product splines to the measured robotic fly data (see Appendix A). Along with the pitch damping coefficient this measurement completes the experimentally determined component of the description of the drift dynamics. When the stroke plane was parallel to the velocity vector, i.e., $\delta = 0$, both f_n and f_t had a negative and approximately linear relationship with speed, indicating the presence of inherent damping in flapping flight to translational velocity perturbations, as has been noted in previous studies (Cheng and Deng, 2011). Both of these force components behaved as if they had a crude, but qualitatively expected, trigonometric relationship with δ for a given speed. The aerodynamic moment results are consistent with what one might expect from a drag force that is linear in velocity and acts on the average center-of-pressure that resides above the center-of-mass, stemming from the similar relationship for f_t. Flies pitch forward (negative ξ by our convention) with increasing velocity (David, 1978), placing them in a regime of the body pitch-moment function that has positive slope. Perturbations in pitch angle would lead to pitch moments in the same direction as the perturbation, leading to a potential instability. However, the coupling of pitch angle and linear velocity gives rise to more interesting dynamics that are not as straightforward and will be explored further.

The moment induced by pitch rotations was approximately linear with rotation rate and independent of the translational body motion. In addition, pitch rotations had a negligible impact on the forces normal and tangential to the stroke plane. We measured the pitch damping coefficient to be, $C_\omega = 1.96 \times 10^2$, in agreement with quasi-steady estimates in previous studies (Cheng et al., 2010). This is roughly a quarter of the passive damping present in yaw rotations (Elzinga et al., 2012; Dickson
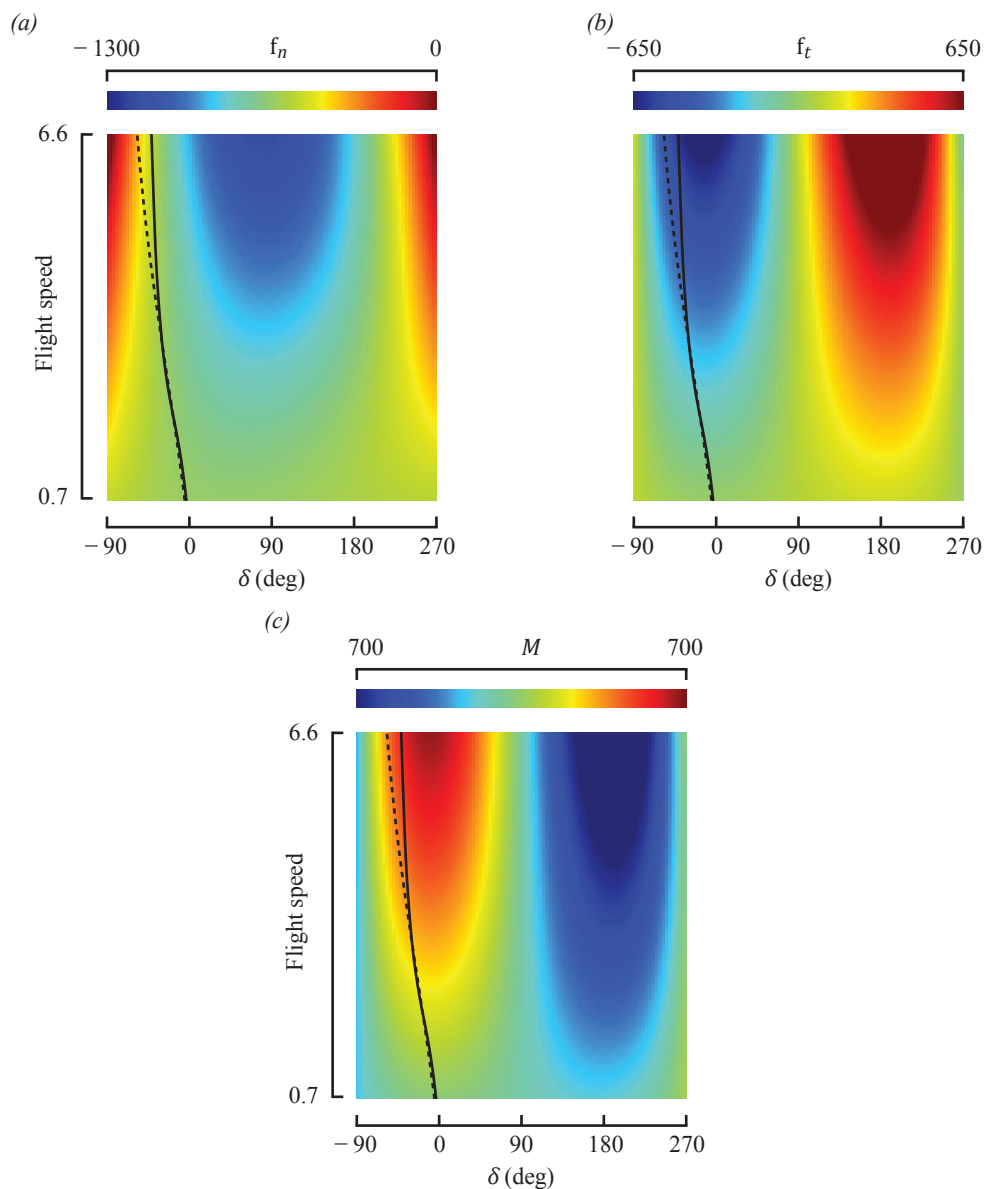
Figure 3.4: Stroke-averaged force and moment maps as a function of δ and flight speed, shown as pseudo color plots for a baseline set of hovering kinematics (Equations 3.10-3.12). The force normal to the stroke plane, *(a)*, the force tangential to the stroke plane, *(b)*, and the pitch moment, *(c)*, are all reported in their dimensionless form with the sign convention defined in Figure 3.2.The body pitch and forward flight speed relationships, $\xi = \psi_1(s)$ and $\xi = \psi_2(s)$, shown in Figure 3.6 are superimposed on all panels.

et al., 2010). The contribution of body drag to the aerodynamic forces and moments was modeled separately based on previous dynamically-scaled model experiments (Dickson et al., 2008). In addition we considered tethered-flight force measurements of body drag in the literature (Vogel, 1966). We found the difference between these measured forces and moments and those due to the components of the robot motor assemblies to be two orders of magnitude smaller than the additional forces on the set of flapping wings due to body motion. Thus, a separate model of the aerodynamic forces on the body was not included in the analysis.

To explore the relationship among body pitch angle, forward flight speed, and their corresponding flight force vector, we computed the compensatory forces and moments required to trim level forward flight (i.e., values of $g_n(\mathbf{u})$, $g_t(\mathbf{u})$, and $N(\mathbf{u})$ such that Equation 3.22 is satisfied) over the relevant range of body pitch angles (0 to $-60°$) and forward flight speeds (0 to 6.6). These results are shown for constant body pitch and constant flight speed curves in Figure 3.5(a)-(c). In practice, the requisite trim forces would need to be generated through the application of some combination of kinematic deformation modes. Based on the observation that body pitch and flight speed are highly correlated in steady-state level forward flight, we narrowed the focus of our analysis to consider two different relationships between body pitch and forward flight speed (Figure 3.6): one derived from published free-flight experiments in flies, $\xi = \psi_1(s)$, and one computed from the body-fixed force vector model posited in the literature, $\xi = \psi_2(s)$ (Vogel, 1966; David, 1978; Götz and Wandel, 1984; Zanker, 1988). In the latter model, the inclination of the force vector is fixed and adjustments in force could only be produced along the direction normal to the stroke plane through stroke amplitude or frequency changes. For body pitch-forward velocity pairs corresponding to both functions, the requisite changes in force production are relatively small. We applied the compensatory forces $g_n(\mathbf{u})$, $g_t(\mathbf{u})$ (shown in Figure 3.5(a)-(b)) to the hovering state force vector ($f_t(0,0) = 0$, $f_n(0,0) = mg$) and plotted resulting force magnitude and orientation in Figure 3.7. The largest force production requirement occurs at hover and subtly decreases with forward speed before reaching a minima near $s = 4.0$. Only at higher speeds is

there an increase in the force production requirement and a change in the ratio of stroke-plane normal to stroke-plane tangential forces that would require significant changes to the wing kinematics. Equilibrium flight speed is largely dictated by the pitch moment, which means that control modes that affect the pitch moment without affecting lift or thrust production may be important.

3.3.2 The role of pitch damping in flight stabilization

We investigated the stability of the drift dynamics by linearizing about a series of operating points for level forward flight (Equation 3.22) and plotting the locus of eigenvalues for the linearized dynamics matrix as the operating point varied with flight speed and the corresponding value of ξ that was given by $\psi_1(s)$, the experimentally observed body pitch and velocity relationship (Figure *3.8(a)*). In all but the fastest flight speeds, we found qualitatively similar natural modes throughout the range of operating points, consisting of both a fast and a slow stable subsistence mode, represented by the two negative real eigenvalues, and an unstable oscillatory mode, represented by the complex conjugate pair of eigenvalues with a positive real part. This is consistent with what has been previously reported in quasi-steady based studies of hovering flight (Cheng and Deng, 2011; Faruque and Humbert, 2010a). As flight speed increases, the complex eigenvalues move towards the real axis until a break-in point is reached and the fast stable eigenvalue retreats further from the imaginary axis.

Additional pitch damping may be implemented in our analysis by allowing $C_\omega = kC_{\omega_0}$ (where C_{ω_0} is the measured damping coefficient and $k > 1$). With a sufficiently high value of k, the system undergoes a supercritical Hopf bifurcation and is stabilized (Figure *3.8(a)*). This result shows that a pitch rate proportional controller, which serves as a pitch damper, is sufficient to stabilize the longitudinal dynamics during level forward flight. Fast mechanosensory feedback of the pitch rate from the halteres into a compensatory wing motor reflex (Dickinson, 1999; Sherman and Dickinson, 2003) would provide just such additional damping (Elzinga et al., 2012).
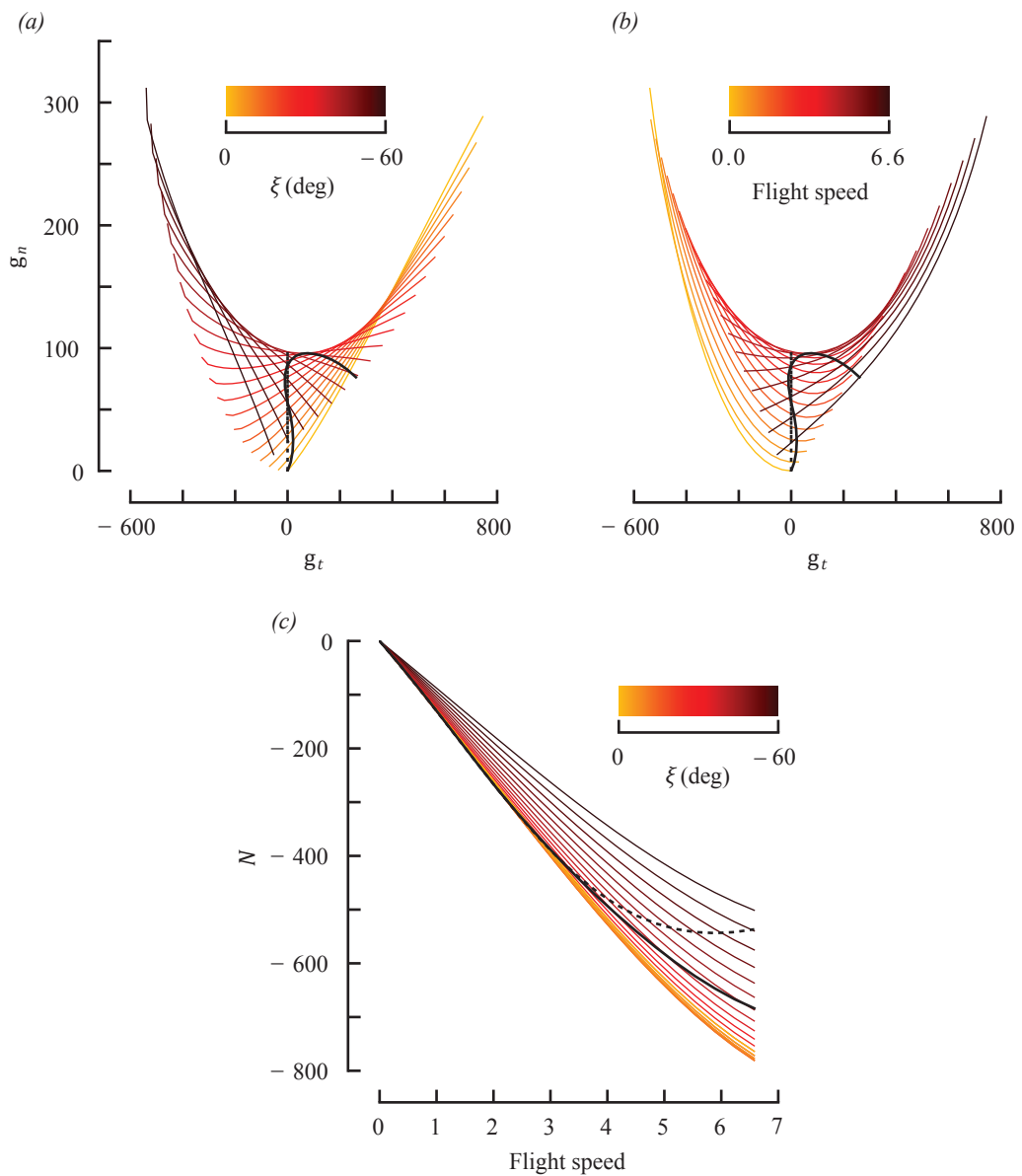
Figure 3.5: Trim forces and moments corresponding to different body pitch angles and flight speeds for level forward flight and a baseline set of hovering wing kinematics, (Equations 3.10-3.12). *(a)* Trim forces tangential to the stroke plane (abscissa) and normal to the stroke plane (ordinate) for lines of constant body pitch with color corresponding to the pitch angle and *(b)* for lines of constant flight speed with color corresponding to the flight speed. *(c)* Pitch moment as a function of flight speed with lines of constant body pitch. Forces and moments in all panels are reported in their dimensionless form with the sign convention defined in Figure 3.2. The body pitch and forward flight speed relationships, $\xi = \psi_1(s)$ and $\xi = \psi_2(s)$, shown in Figure 3.6 are superimposed on all panels.
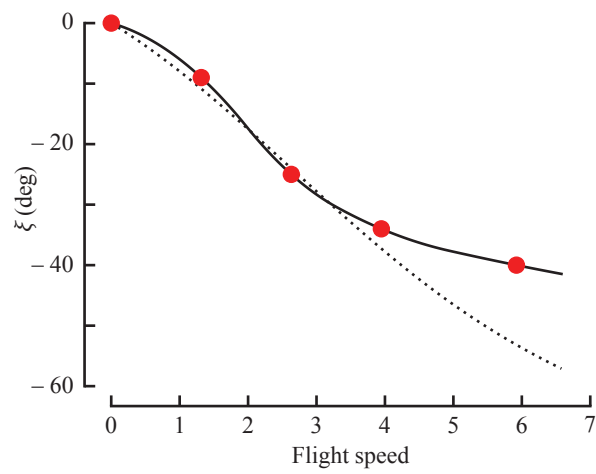
Figure 3.6: Relationship between body pitch angle and forward flight speed, for published data, $\xi = \psi_1(s)$ (data points in red with interpolation spline in solid black (David 1978)), and computed from the condition where forces tangential to stroke plane are balanced without additional wing kinematic changes, $\xi = \psi_2(s)$ (dashed line).
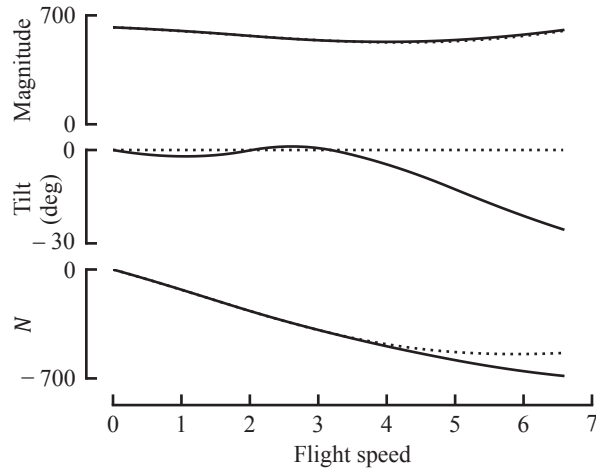
Figure 3.7: Flight force vector and pitch moment for the body pitch-to-flight speed relationships, $\xi = \psi_1(s)$ and $\xi = \psi_2(s)$, depicted in Figure 3.6.

As flight speed increases, the damping requirement for stability rises as well (Figure 3.8(b)), suggesting a control design that might benefit from tuning controller gains as a function of forward velocity. This notion is an example of a more general method of nonlinear control system design referred to as gain scheduling (Khalil, 1996). The results were similar when considering instead the velocity and body pitch pair given by $(s, \psi_2(s))$, but with a larger damping requirement at the high end of the flight speed range.

3.3.3   Stroke-averaged forces and moments for the deformation modes

The stroke-averaged aerodynamic forces and moments as a function of the deformation parameter for each of the three kinematic deformation modes are shown alongside time series plots of their associated wing kinematic variables in Figure 3.9. Each deformation mode generated a pitch moment that was approximately linear with
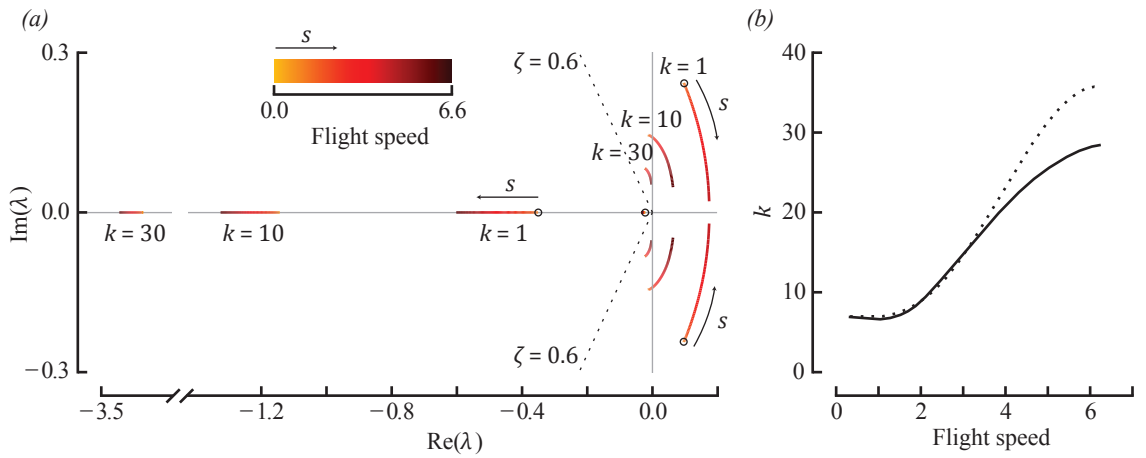
Figure 3.8: Eigenvalues and stabilization damping for the linearized dynamics at different flight speeds. *(a)* Eigenvalues (λ_i) of the linearized dynamics at different flight speeds and pitch damping values. The body pitch used for each operating point was a function of flight speed as given by the observed relationship in free-flight, $\xi = \psi_1(s)$ (Figure 3.6, (David, 1978)). Color corresponds to the flight speed of each operating point. Grey lines depict the real and imaginary axes. The location of an eigenvalue relative to the imaginary axis dictates the stability of the subspace spanned by its corresponding eigenvector. The dotted line indicates a damping factor of $\zeta = \frac{Re(\lambda_i)}{|\lambda_i|} = 0.60$, which is a reference for the characterization of the dominant poles of the system. *(b)* k, the pitch damping given as a multiple of the passive damping, that stabilizes the dynamics as a function of flight speed for both body pitch and velocity relationships, $\xi = \psi_1(s)$ and $\xi = \psi_2(s)$, shown in Figure 3.6.

respect to the deformation parameter over a significant range within the morphological bounds of their input. Because the parameterization of the input for each control mode is somewhat arbitrary, comparing the slope of the response for each mode offers little quantitative insight, but the mean stroke offset mode did provide the largest moment response over the extent of its linear range. Both the mean stroke offset mode and the differential deviation mode produced a pitch moment without significantly altering the flight forces, whereas the wing rotation mode reduced the force component normal to the stroke plane while contributing to the tangential force. This suggests that the wing rotation mode could play a useful role in trimming flight forces at higher speeds where a change in the ratio of stroke-plane normal to stroke-plane tangential force is required for the observed velocity and body pitch relationship.

We explored the state dependence of the pitch moment for the mean stroke offset mode and the differential deviation mode, the two modes that did not significantly affect the tangential and normal forces, to determine if there were any distinguishing performance features. We conducted two additional constant velocity translation experiments at incremented body pitch values for a set of wing kinematics with a constant input for each of the deformation modes. The aerodynamic moment as a function of δ and s was measured for each deformation mode case and, after subtracting the baseline, yielded the pseudo color plots in Figure *3.10(a) and (b)*. As s increased, the pitch moment response at the corresponding body pitch given by both $\psi_1(s)$ and $\psi_2(s)$ was amplified for the differential deviation mode, in contrast to the mean stroke offset mode which exhibits some variation but much less of a persistent trend with increasing flight speed (Figure *3.10(c)*). This result suggests a possible mechanism to cope with the velocity-dependent damping requirement if the differential deviation mode was used in realizing a pitch rate proportional controller which stabilizes the longitudinal dynamics.
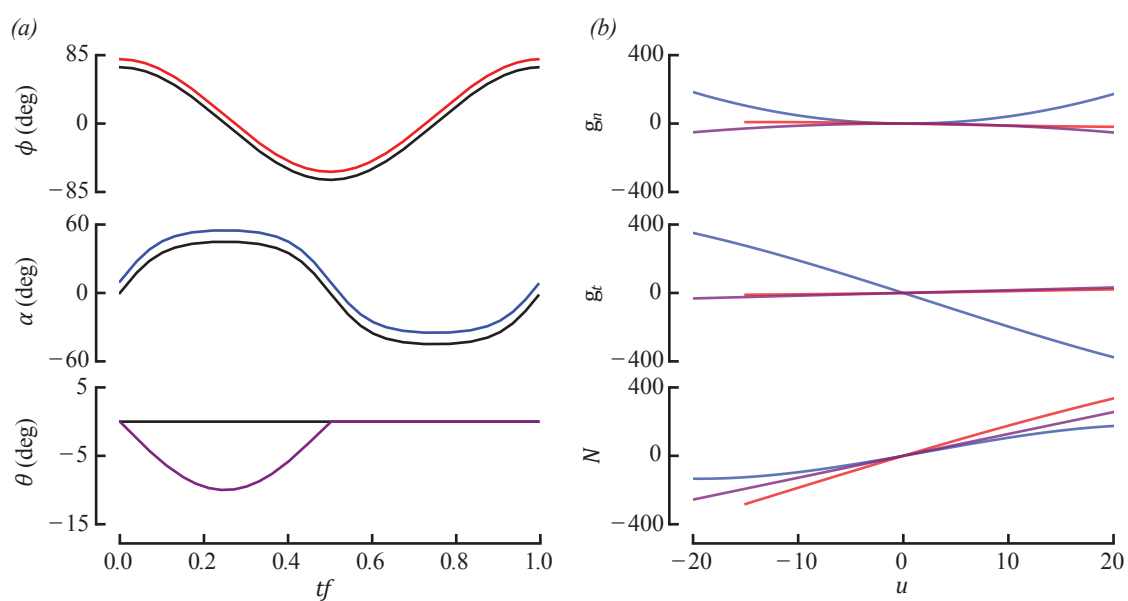
Figure 3.9: Kinematic deformation modes and their stroke-averaged force and moment production. *(a)* Wing kinematics for a representative positive deformation parameter for the mean stroke offset mode, u_{ms} (red), the wing rotation mode, u_{wr} (blue), and differential deviation mode, u_{dd} (purple). *(b)* Polynomial fits of the baseline (nominal hovering kinematics) subtracted stroke-averaged forces and moments as a function of deformation parameter for each of the three kinematic deformation modes with colors consistent with panel *(a)*.
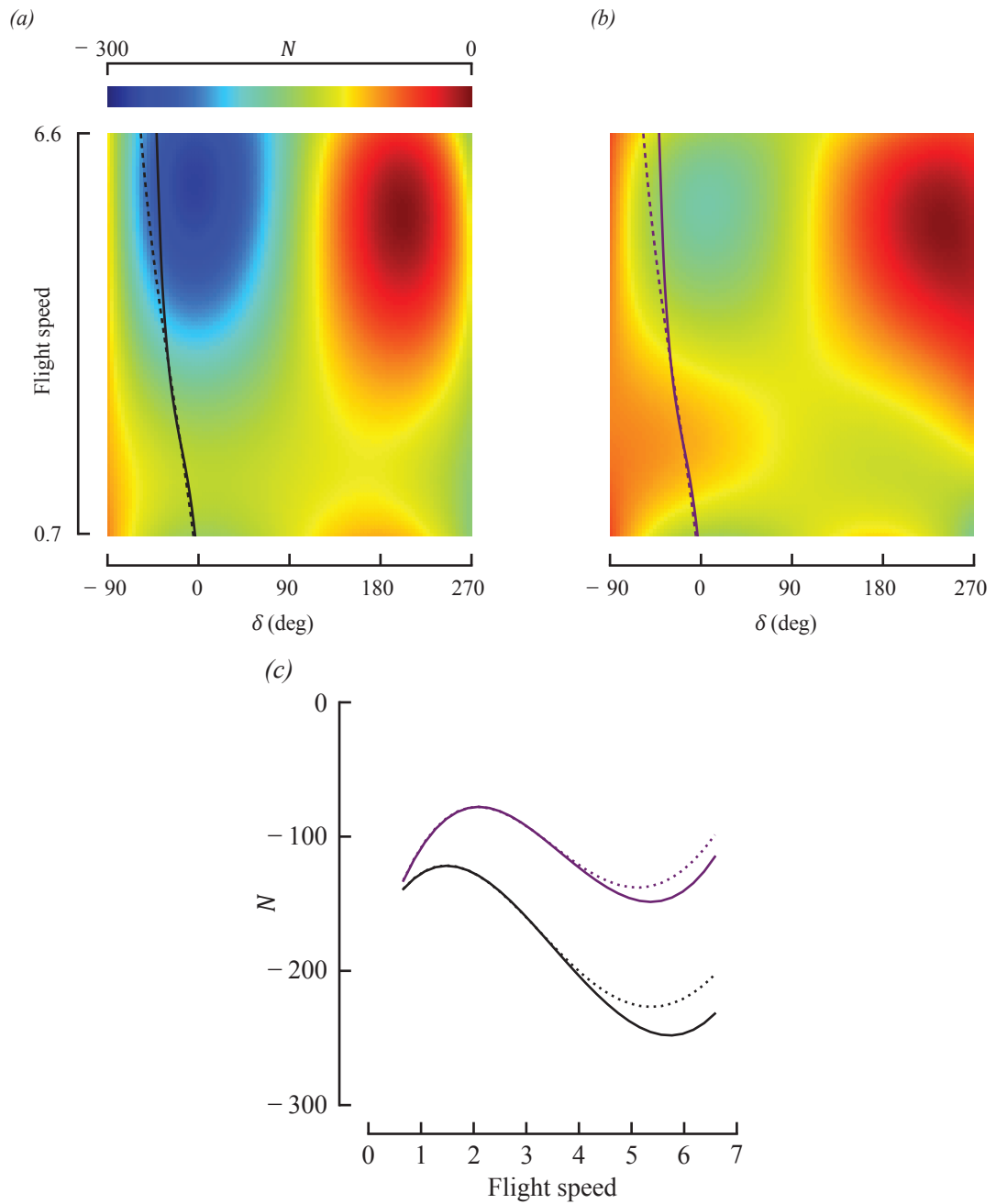
Figure 3.10: State dependence of the pitch moment generated by the differential deviation and mean stroke offset kinematic deformation modes. *(a)* Stroke-averaged pitch moment map as a function of δ and flight speed after subtracting the contribution of the baseline kinematics yielding a state dependent N. This is shown as a pseudo color plot for a single deformation parameter value of the differential deviation mode and (b) for the mean stroke offset mode. (c) N as a function of flight speed for both pitch body pitch and velocity relationships, $\xi = \psi_1(s)$ and $\xi = \psi_2(s)$, shown in Figure 3.6, with the kinematic deformation mode color coordinated with panels (a) and (b).

3.4 Discussion

The results of this study indicate that equilibrium flight speed is largely dictated by the pitch moment. This implies flies may employ control modes that affect the pitch moment without affecting lift or thrust production, such as the mean-stroke offset control mode. At high speeds, both additional pitch torque and a flight force tilt are required, which implicates the wing rotation control mode. The results also show that a pitch rate proportional controller, which serves as a pitch damper, is sufficient to stabilize body pose during forward flight. The damping requirement is velocity dependent and increases with flight speed. Fast mechanosensory feedback of pitch rate from the halteres could enable active damping and would exhibit inherent gain scheduling with flight speed if the pitch torque was generated by the differential deviation deformation mode. We hypothesize that differences between upstroke and downstroke deviation likely play a critical role in flight stabilization across a wide range of flight speeds. The roles suggested for each of the deformation modes in trimming flight forces and stabilizing the dynamics of level forward flight in flies are summarized in Figure 3.11.

3.4.1 Interpreting the flight force vector

Several experimental lines of evidence support the notion that flies alter the magnitude, but not the direction, of their flight force vector relative to their body orientation and that body pitch is primarily responsible for controlling the direction of force output. This phenomenon was observed in optomotor control experiments in tethered *Drosophila* performed in still air (Götz and Wandel, 1984). In this model, the covariance of force components would be achieved through stroke amplitude changes which would increase the size of an actuator disk defined by the area swept out by the wings during a stroke (Zanker, 1988; Ellington, 1984a). Stroke frequency also plays a role, but is less variable on a wing stroke to wing stroke basis (Lehmann and Dickinson, 1997). The force vector would be tilted forward via body pitch to balance drag in forward flight and the magnitude of the force vector would increase with the secant of
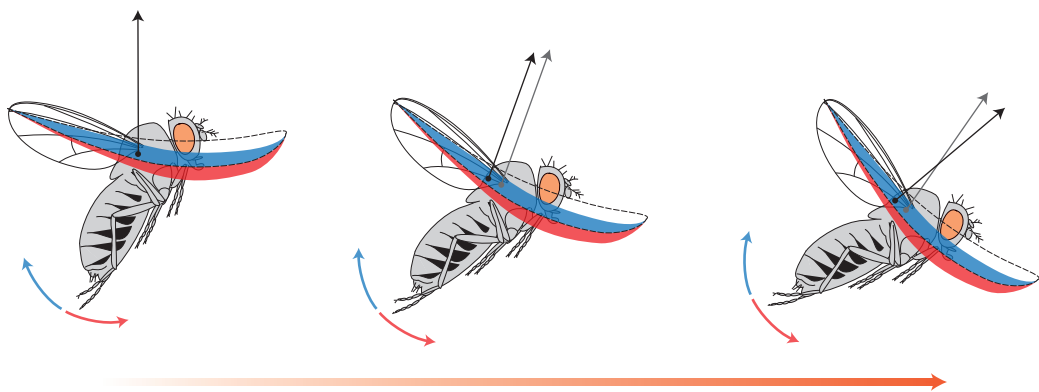
Figure 3.11: Illustrative summary of hypothesized wing kinematic changes associated with trimming and stabilizing level forward flight in flies. The flight force vector is shown in black and compared to the flight force vector for the hovering state (grey). As flight speed increases (shown from left to right) the animal pitches forward. At low to mid speeds the pitch moment required to balance the moment due to body motion is generated through shifting the force vector back by utilizing the mean stroke offset mode and the overall force production is slightly reduced with stroke amplitude changes. At high speeds, the requisite additional pitch torque and tilting of the force vector is accomplished through the wing rotation mode. Across all speeds, active damping is achieved through proportional feedback of the pitch rate to torque produced by means of the differential deviation mode. The pitch rotations indicated by the colored arrows correspond to the like color changes in deviation of the wing stroke.

body pitch to maintain weight support. The interpretation of the flight force vector is straightforward in still air or when there is a clear separation between the source of propulsion and the lift and drag producing surfaces, such as in a conventional aircraft. The notion of a flight force vector in forward flight for an insect is complicated by changes in airspeed and the associated additional forces acting on the wings due to body motion, which are much more important than the parasitic drag on the body itself. We define the flight force vector as the superposition of the compensatory trim forces $(g_t(\mathbf{u}), g_n(\mathbf{u}))$ and the hovering state force vector $(f_t(0,0), f_n(0,0))$, as shown in Figure 3.7. We interpret the state dependent forces that result in lift and drag forces due to body motion as $(f_t(\delta, s) - f_t(0,0), f_n(\delta, s) - f_n(0,0))$.

The observation of the animal pitching its body forward as flight speed increased was noted by Vogel during tethered flight experiments where he adjusted the airspeed in a wind tunnel to achieve a thrust balance and determine the preferred airspeed of the animal at a given body pitch orientation (Vogel, 1966). This relationship between body pitch and flight speed was measured in free flight by David and confirmed Vogel's findings (David, 1978). The relationship was indeed qualitatively consistent with the fixed force vector inclination observed by Götz, but the difficulties in defining the force vector in the presence of a non-zero airspeed do not permit an explicit comparison. David assumed that an increase in the force vector magnitude would be required to yield weight support at the observed body pitch angle changes and computed drag forces based on this assumption. Contrary to this intuition, our results suggest that the vertical lift is enhanced from the body velocity and this is sufficient not only to make up the deficit resulting from forward pitching but to slightly reduce the magnitude of the force requirement over the low-to-mid forward velocity range. In many ways, this is not as surprising after considering the large instantaneous forces produced tangentially to the stroke plane during hovering on the upstroke and downstroke that are a wasted byproduct of sufficient lift production. We also note that this is reminiscent of Pennycuick's prediction of a u-shaped relationship between power and flight speed (Pennycuick 1968). Whereas we did not observe an increase in requisite force production to maintain weight support, a fixed inclination of the flight

force vector does appear to be maintained at the body pitch and forward velocity relationship observed in free flight for flight speeds of less than 4.0, as indicated by negligible trim forces tangential to the stroke plane within this range (Figure 3.7).

3.4.2   On the role of shifts in the mean spanwise rotation angle of the wing

Recent studies based on free-flight observations and quasi-steady simulations have suggested that the control of forward flight speed in *Drosophila* is mediated by changes in the mean spanwise rotation angle of the wing (Ristroph et al., 2011). This, along with documented evidence of the involvement of bilateral asymmetries in this parameter during yaw turns and further support for the mechanism in hawkmoths, provided the inspiration for the wing rotation deformation mode considered in this study (Cheng et al., 2011; Fry et al., 2003; Hedrick et al., 2009; Bergou et al., 2009). Our results suggest that in flies this mechanism is most important for $s > 4.0$. The highest speed trajectories observed by Ristroph and colleagues is near this transition, but they noted the importance of the mean spanwise rotation angle at low speeds as well. There are a few possible explanations for this discrepancy. Changes in body pitch (which were not reported) would enter into the spanwise wing rotations recorded in the lab frame coordinates used in their study. From an aerodynamic and modeling perspective, the choice of coordinates in defining the wing kinematics is immaterial, but it has important consequences in interpreting the animals' response. A second possibility is a small disparity between the recorded sequences and true steady-state level forward flight conditions. In confined flight arenas, there is a high probably of maneuvering flight bouts through the capture volume. Their analysis was limited to accelerations of less than $0.15g$, but this could still result in sizable excursions in the state variables (Figure 3.5).

At higher flight speeds our results suggest a forward tilt of the force vector is required to trim the flight forces associated with the observed free-flight relationship of body pitch and forward flight speed, which could be achieved through the utilization

of the wing rotation mode. Because this phenomenon was not observed for optomotor control experiments in still air (Götz and Wandel, 1984), it is possible that the shift in mean rotation angle at high speeds is a passive consequence of the deformable nature of the wing hinge and the upstroke to downstroke differences in the local velocity field during forward flight. Another hypothesis is that such a mode is not activated until the detection of a sufficiently high airspeed through another sensory modality.

3.4.3 Gain scheduling during active damping

Analysis of the longitudinal flight dynamics of level forward flight in flies revealed an unstable mode that persisted throughout the range of flight speeds considered in this study (Figure 3.8). The results show that the dynamics may be stabilized with sufficiently high pitch damping at any given forward flight speed. Additional damping may be provided actively by a pitch rate proportional controller implemented via a haltere-motor reflex (Dickinson, 1999; Sherman and Dickinson, 2003; Elzinga et al., 2012). Stabilization using fast inner-loop feedback would remove restrictions imposed by right half planes poles (Aström and Murray, 2010) for a slower visually-mediated outer-loop controller.

The stability result is, however, local to a neighborhood around the operating point because the analysis was performed via linearization. We approach the nonlinear dynamics by noting how the linearized dynamics change with the operating point: as flight speed increases, the damping requirement for stability also rises (Figure 3.8(b)). We utilize the forward velocity magnitude as a scheduling variable and consider a family of linear pitch rate proportional controllers parameterized by the magnitude of forward velocity, a technique called gain scheduling (Khalil, 1996). The damping term in Equation 3.21 becomes:

$$c_\omega = (C_{\omega_0} - bC_{u_i}), \tag{3.24}$$

where C_{u_i} is the actuation coefficient for a given deformation mode,

$$C_{u_i} = \left. \frac{\partial N}{\partial u_i} \right|_{u_i=0},$$ (3.25)

and b is the gain,

$$b = \frac{C_{\omega_0}}{C_{u_i}}(1 - k(s)).$$ (3.26)

The damping multiple as a function of forward speed required for stability, $k(s)$, is shown in Figure 3.8(b). We assume the sensorimotor delay in the haltere circuit to be low enough to allow for a sufficient level of active damping (Elzinga et al., 2012), but delays in the measurement of the scheduling variable from other sensory modalities used in modulating the feedback gain might be problematic. The animal could utilize a constant gain strategy across all flight speeds, corresponding to the peak damping value, but overly damped dynamics at low speeds may have consequences for maneuverability. To explore the consequences of a delayed measurement of the scheduling variable we simulated the response of the fly to a $20\,\mathrm{cm} \cdot \mathrm{s}^{-1}$ horizontal velocity perturbation and numerically solved the set of delayed differential equations using software written in Python. The simulation code relied heavily on the Pydelay package which implements an algorithm based on the Bogacki-Shampine method (Flunkert and Schoell, 2009). We assumed the following form for the damping function:

$$k(s) = k_0(s) + c\left(\sup_{0 \le s \le 6.6} k_0(s) - k_0(s) \right), \qquad c \in [0, 1],$$ (3.27)

which was deduced from the limiting cases of: 1) an infinite delay, where accurate information regarding the flight speed cannot be garnered and the constant gain strategy must be used, and 2) a zero delay, where $k(s) = k_0(s)$. Using this assumption, we determined the damping multiple required to stabilize the dynamics as a function of the flight speed for a feedback gain which was modulated using a delayed estimate of the forward velocity. The results are shown in Figure 3.12 for several delays ranging from 1 to 10 wing strokes, which encompass the approximate visual-motor delay
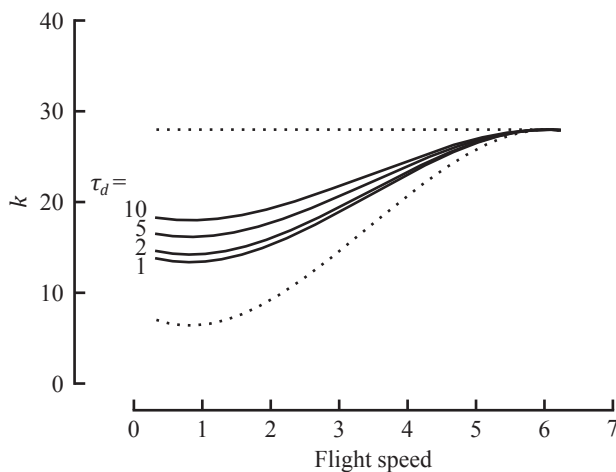
Figure 3.12: Pitch damping (given as a multiple of the passive damping) required to stabilize the dynamics as a function of the flight speed when tuning the feedback-based damping using a delayed estimate of the forward velocity. Damping values were determined through simulation of the delayed differential equations and by assuming the same functional form for the damping-velocity relationship as determined in the undelayed case. Dashed lines represent the stabilization damping for the undelayed and the infinite delay cases. The delay in measuring forward velocity, τ_d, is reported in wing strokes.

of 7 wing strokes (Land and Collett, 1974; Roth et al., 2012). This suggests that flies would benefit from using an actuation mode such as the differential deviation mode for feedback-based pitch damping, which has greater authority at higher airspeeds (Figure 3.10) without being subject to additional sensor delays. This provides an elegant solution for flight stabilization across a wide range of flight speeds and may be an example of a more general theme in fly flight control where some of the computational complexity is offloaded to the mechanics as a way combating performance limits imposed by sensory delays. We hope to explicitly test this hypothesis in the future with measurements of time resolved wing kinematics during mechanical perturbations performed on tethered flies in a wind tunnel.

Chapter 4

Conclusion

Insects were the first animals to evolve active flight and remain unsur-
passed in many aspects of aerodynamic performance and maneuverability.

—Michael Dickinson (1999)

Flies are incredibly robust fliers. Whether they are subjected to wing damage, mid-air collisions, or wind gusts on par with their top airspeed, flies are able to sustain stable flight and still manage to do so despite a small computational budget and long sensorimotor delays relative to their flight dynamics. In principle, achieving high performance in the presence of long delays would imply the need for high fidelity forward models. Reliance on the accuracy of such models would, however, lead to increased fragility. Flies appear particularly adept at balancing the competing demands of delay tolerance, performance, and robustness which invites thoughtful examination of their multimodal feedback architecture. This dissertation examined stabilization requirements for inner-loop feedback strategies in flapping flight for *Drosophila* against the backdrop of sensorimotor transformations present in the animal. This was achieved through experimental characterization of the passive flight dynamics and changes in wing kinematics using a dynamically-scaled robot along with subsequent analysis within a control theoretic framework. Here we summarize the main results of this thesis, develop some unifying conclusions about the role of mechanosensory feedback in insect flight control, and discuss future work to build upon these findings.

4.1 Summary of findings

In Chapter 2, we studied the dynamics of hovering yaw turns during flapping flight and the impact of sensory delays on the stability and performance of feedback reflexes during a stereotyped body saccade for a fruit fly. To perform this analysis, we utilized a dynamically-scaled robotic model with captive trajectory capability about the yaw axis. Yaw torque was controlled through a deformation in the wing kinematics which resulted in bilateral asymmetries in the angle of attack. System characterization experiments for a range of feedback delays similar in dimensionless timescale to those present in the nervous system agreed with relatively simple stroke-averaged models based on measurements of the passive dynamics and actuation torques generated by changes in wing kinematics. The simplicity of the stroke-averaged model and its close agreement with captive trajectory experiments afforded the opportunity to gain fundamental insights through closed-form solutions. The results demonstrate that a proportional controller decreases the system time constant by adding an active damping component, but is constrained by a tradeoff between sensor delay and permissible feedback gain. The open-loop yaw velocity dynamics are passively stable, but time delays consistent with those present in a fly's nervous system are sufficient to destabilize the closed-loop system for high enough gain. When considering the fly's proportional response to wide-field visual motion during tethered flight in isolation, that is, only accounting for passive damping characteristics and neglecting the high-frequency roll-off of the visual response, the identified controller is indeed unstable given the long delay of the visual system. In addition to the importance of the low-pass filter characteristics of the visual system, this suggests that the role of the haltere may be to provide fast inner-loop feedback, resulting in additional active damping which would allow the slower visual system to operate at higher gain with a faster response for the same level of robustness. A yaw rate stabilization reflex consisting of an inner-loop proportional controller from haltere feedback that provides additional damping for an outer-loop visual low-pass filter is consistent with open-loop measurements in tethered flight and provides performance and robustness

characteristics expected by engineering design principles. The low cut-off frequency of the visual system, which is necessarily low due to the permissible cross-over frequency resulting from the visual system delay, explains why visual responses during saccades and other fast maneuvers are not prominent. This analysis also provides evidence that the large open-loop responses observed in tethered-flight might not be an artifact of the preparation, as previously suggested, but, in the proper context, are the expected open-loop responses of a properly designed flight control system.

In Chapter 3 we modified the dynamically-scaled robotic apparatus to study how flies adjust stroke features to regulate and stabilize level forward flight in the longitudinal plane. The results suggest that few changes to hovering kinematics are necessary to meet steady-state lift and thrust requirements at different flight speeds when following the experimentally observed relationship between body pitch and flight speed. The equilibrium flight speed is instead largely dictated by the pitch moment which implies flies may employ control modes that affect the pitch moment without affecting lift or thrust production, such as the mean-stroke offset control mode. This finding is consistent with prior hypotheses based on tethered-flight force measurements and free-flight observations. At higher speeds, however, force production tangential to the stroke plane is required in addition to trimming the pitch moment, which implicates the wing rotation control mode. The results also show that the dynamics may be stabilized with the addition of a pitch damper, but that the magnitude of required damping increases with flight speed. We posit that differences in stroke deviation between the upstroke and downstroke might play a significant role in this stabilization. Low latency mechanosensory feedback of the pitch rate from the halteres could provide damping, which would inherently exhibit gain scheduling with flight speed if pitch torque is regulated by adjusting stroke deviation. Stroke deviation is a parameter that has largely been treated as insignificant in the literature, but changes in stroke deviation have been correlated with steering muscle activation and utilizing such a control scheme would provide an elegant solution for flight stabilization across a wide range of flight speeds.

Visually guided flight performance in flies is limited by the permissible cross-

over frequency arising from the long visuomotor delay, leading to constraints on the underlying dynamics to ensure controllability. For hovering yaw dynamics, added rotational damping was desirable and for longitudinal forward flight it was required. In both cases, hind wings would presumably provide larger passive damping, whereas low latency rate sensors given by halteres would allow for a larger amount of active damping. The conservation of overall damping characteristics may very well have played a crucial role in the evolution of the haltere from the hind wing. Similarly, sensory feedback-based linear damping is present in antennae-mediated responses to airspeed changes. Dipteran flight performance most likely benefits from this trading of passive damping for fast mechanosensory feedback loops that provide active damping. More generally, we see a hierarchical control structure emerge to balance performance and robustness in response to significant sensorimotor delays which persist, despite numerous evolutionary specializations, due to neurobiological constraints.

4.2 Future directions

The characterization of flight dynamics in *Drosophila* presented in this dissertation will allow for a theoretical treatment of higher-level control strategies as well as place task-level behavioral experiments in the proper context of the animal's underlying flight dynamics. A number of laboratories, including our own, are exploring this topic in free-flight using automated computer vision-based tracking at the level of both body kinematics and wing kinematics to measure responses to both visual and mechanical perturbations. Free-flight experiments provide a more naturalistic setting to explore these phenomena and understanding natural behavior is the end-game, but tethered-flight experiments still present an opportunity to isolate behavioral responses for a particular modality in a more straight-forward manner. System identification experiments in tethered flies subjected to mechanical oscillations, similar to Sherman and Dickinson (2003), with subtle physical manipulations of the haltere end-knob could serve to further elucidate the role of the haltere in providing additional damping. Physical manipulations of the haltere have been performed before with some success,

but manipulating the haltere gain without affecting critical resonant properties is not trivial. The hypotheses put forth here regarding the role of several deformation modes of the wing kinematics in stabilizing longitudinal forward flight may be addressed in tethered flies enclosed in a low-speed wind tunnel using high-speed video to record changes in wing kinematics. This apparatus would additionally require a motor-controlled rotational degree of freedom to set the pitch angle as a function of airspeed and provide a means to introduce mechanical perturbations. Finally, incorporating a vertical degree of freedom into the robotic fly apparatus would complete its captive trajectory capability in the longitudinal plane and would allow experiments to fully validate stroke-averaged simulations far from equilibria. The ultimate goal in the study insect flight is to bridge multiple layers of analysis to understand how sensory information is processed, how muscle activation leads to wing kinematic changes through musculoskeletal mechanics, and how changes in wing and body kinematics generate aerodynamic forces. As we make progress in these areas, we develop a better understanding of insect flight control strategies, gain insight into the neural basis of behavior, and find inspiration for micro-air vehicle designs.

Bibliography

Aström, K. J. and Murray, R. M. (2010). *Feedback Systems: An Introduction for Scientists and Engineers.* Princeton University Press.

Autrum, H. (1958). Electrophysiological analysis of the visual systems in insects. *Experimental Cell Research*, 14(Suppl 5):426–439.

Balint, C. N. and Dickinson, M. H. (2001). The correlation between wing kinematics and steering muscle activity in the blowfly Calliphora vicina. *The Journal of Experimental Biology*, 204(Pt 24):4213–26.

Balint, C. N. and Dickinson, M. H. (2004). Neuromuscular control of aerodynamic forces and moments in the blowfly, Calliphora vicina. *The Journal of Experimental Biology*, 207(Pt 22):3813–38.

Bender, J. a. and Dickinson, M. H. (2006a). A comparison of visual and haltere-mediated feedback in the control of body saccades in Drosophila melanogaster. *The Journal of Experimental Biology*, 209(Pt 23):4597–606.

Bender, J. A. and Dickinson, M. H. (2006b). Visual stimulation of saccades in magnetically tethered Drosophila. *The Journal of Experimental Biology*, 209(Pt 16):3170–3182.

Bergou, A. J., Ristroph, L., Guckenheimer, J., Cohen, I., and Wang, Z. J. (2009). Fruit flies modulate passive wing pitching to generate in-flight turns. *Physical Review Letters*, 104(14):148101.

Berman, G. J. and Wang, Z. J. (2007). Energy-minimizing kinematics in hovering insect flight. *Journal of Fluid Mechanics*, 582:153.

Blondeau, J. and Heisenberg, M. (1982). The three-dimensional optomotor torque system of Drosophila melanogaster. *The Journal of Comparative Physiology*, 145(3):321–329.

Braitenberg, V. (1967). Patterns of projection in the visual system of the fly. I. Retina-lamina projections. *Experimental Brain Research*, 3(3):271–298.

Burkhardt, D. and Gewecke, M. (1965). Mechanoreception in Arthropoda: the chain from stimulus to behavioral pattern. *Cold Spring Harb. Symp.*, 30:601–614.

Burrows, M. (1996). *The Neurobiology of an Insect Brain.* Oxford University Press, Oxford.

Butcher, J. C. (2008). *Numerical methods for ordinary differential equations.* Numerical algorithms. Wiley.

Chan, W. P. and Dickinson, M. H. (1996). Position-specific central projections of mechanosensory neurons on the haltere of the blow fly, Calliphora vicina. *Journal of Comparative Neurology*, 369(3):405–418.

Chan, W. P., Prete, F., and Dickinson, M. H. (1998). Visual Input to the Efferent Control System of a Fly's "Gyroscope". *Science*, 280(5361):289–292.

Cheng, B. and Deng, X. (2011). Translational and rotational damping of flapping flight and its dynamics and stability at hovering. *Robotics, IEEE Transactions on*, 27(5):849–864.

Cheng, B., Deng, X., and Hedrick, T. L. (2011). The mechanics and control of pitching manoeuvres in a freely flying hawkmoth (Manduca sexta). *The Journal of Experimental Biology*, 214(24):4092–4106.

Cheng, B., Fry, S. N., Huang, Q., and Deng, X. (2010). Aerodynamic damping during rapid flight maneuvers in the fruit fly Drosophila. *The Journal of Experimental Biology*, 213(4):602–12.

Cowan, N. J., Lee, J., and Full, R. J. (2006). Task-level control of rapid wall following in the American cockroach. *The Journal of Experimental Biology*, 209(Pt 9):1617–29.

David, C. (1978). The relationship between body angle and flight speed in free-flying Drosophila. *Physiological Entomology*, 3:191–195.

Derham, W. (1714). *Physico-theology.* W. Innys., London.

Dickinson, M. H. (1999). Haltere-mediated equilibrium reflexes of the fruit fly, Drosophila melanogaster. *Philosophical transactions of the Royal Society of London. Series B, Biological sciences*, 354(1385):903–16.

Dickinson, M. H. (2006). Insect flight. *Current Biology*, 16(9):R310.

Dickinson, M. H., Farley, C. T., Full, R. J., Koehl, M. A. R., Kram, R., and Lehman, S. (2000). How Animals Move: An Integrative View. *Science*, 288(5463):100–106.

Dickinson, M. H., Lehmann, F.-O., and Sane, S. P. (1999). Wing rotation and the aerodynamic basis of insect flight. *Science*, 284(5422):1954–60.

Dickinson, M. H. and Tu, M. (1997). The function of dipteran flight muscle. *Comparative Biochemistry and Physiology A: Physiology*, 116(3):223–238.

Dickson, W. B. and Dickinson, M. H. (2004). The effect of advance ratio on the aerodynamics of revolving wings. *The Journal of Experimental Biology*, 207(Pt 24):4269–81.

Dickson, W. B., Polidoro, P., Tanner, M. M., and Dickinson, M. H. (2010). A linear systems analysis of the yaw dynamics of a dynamically scaled insect model. *The Journal of Experimental Biology*, 213(17):3047–3061.

Dickson, W. B., Straw, A. D., and Dickinson, M. H. (2008). Integrative Model of Drosophila Flight. *AIAA Journal*, 46(9):2150–2164.

Egelhaaf, M. and Borst, A. (1993). movement detection in arthropods. *Rev. Oculo-mot. Res.*, 5:55–77.

Ellington, C. (1984a). The aerodynamics of hovering insect flight. I. The quasi-steady analysis. *Philosophical Transactions of the Royal Society B: Biological Sciences*, 305:1–15.

Ellington, C. (1984b). The aerodynamics of hovering insect flight. III. Kinematics. *Philosophical Transactions of the Royal Society*, 305(1122):41–78.

Ellington, C., Van Den Berg, C., Willmott, A. P., and Thomas, A. L. R. (1996). Leading-edge vortices in insect flight. *Nature*, 384(6610):626–630.

Elzinga, M. J., Dickson, W. B., and Dickinson, M. H. (2012). The influence of sensory delay on the yaw dynamics of a flapping insect. *Journal of the Royal Society Interface*, 9(72):1685–1696.

Elzinga, M. J., Van Breugel, F., and Dickinson, M. H. (In review). Wing kinematics and the stabilization of longitudinal forward flight in flies.

Ennos, A. (1989). The Kinematics and aerodynamics of the Free Flight of some Diptera. *The Journal of Experimental Biology*, 85:49–85.

Epstein, M., Waydo, S., Fuller, S. B., Dickson, W. B., Straw, A., Dickinson, M. H., and Murray, R. M. (2007). Biologically Inspired Feedback Design for Drosophila Flight. *2007 American Control Conference*, pages 3395–3401.

Etkin, B. and Reid, L. D. (1998). *Dynamics of Flight; Stability and Control.* John Wiley & Sons, New York, third edition.

Faruque, I. and Humbert, J. S. (2010a). Dipteran insect flight dynamics. Part 1 Longitudinal motion about hover. *Journal of Theoretical Biology*, 264(2):538–552.

Faruque, I. and Humbert, J. S. (2010b). Dipteran insect flight dynamics. Part 2: Lateral-directional motion about hover. *Journal of Theoretical Biology*, 265(3):306–313.

Fayyazuddin, A. and Dickinson, M. H. (1996). Haltere afferents provide direct, electrotonic input to a steering motor neuron in the blowfly, Calliphora. *Journal of Neuroscience*, 16(16):5225–5232.

Flunkert, V. and Schoell, E. (2009). Pydelay - a python tool for solving delay differential equations. *Arxiv Preprint*, 3(2).

Fontaine, E. I., Zabala, F. A., Dickinson, M. H., and Burdick, J. W. (2009). Wing and body motion during flight initiation in Drosophila revealed by automated visual tracking. *The Journal of Experimental Biology*, 212(Pt 9):1307–1323.

Fox, J. L. and Daniel, T. L. (2008). A neural basis for gyroscopic force measurement in the halteres of Holorusia. *Journal of Comparative Physiology A*, 194(10):887–897.

Fraenkel, G. (1939). The function of the halteres of flies (Diptera). *Proc. Sool. Soc. Lond. A*, 109:69–78.

Fry, S. N., Rohrseitz, N., Straw, A. D., and Dickinson, M. H. (2009). Visual control of flight speed in Drosophila melanogaster. *Journal of Experimental Biology*, 212(Pt 8):1120–1130.

Fry, S. N., Sayaman, R., and Dickinson, M. H. (2003). The aerodynamics of free-flight maneuvers in Drosophila. *Science*, 300(5618):495–498.

Frye, M. a. (2010). Multisensory systems integration for high-performance motor control in flies. *Current opinion in neurobiology*, 20(3):347–52.

Frye, M. A. and Gray, J. R. (2005). Mechanosensory Integration for flight control in insects. In Christensen, T. A., editor, *Methods in insect sensory neuroscience*, chapter Mechanosen, pages 107–128.

Fuller, S. B. (2011). *Visual Autocorrelators and Antenna-mediated Airspeed Feedback in the Control of Flight Dynamics in Fruit Flies and Robotics*. PhD thesis, California Institute of Technology.

Gao, N., Aono, H., and Liu, H. (2011). Perturbation analysis of 6DoF flight dynamics and passive dynamic stability of hovering fruit fly Drosophila melanogaster. *Journal of Theoretical Biology*, 270(1):98–111.

Götz, K., Hengstenberg, B., and Biesinger, R. (1979). Optomotor control of wing beat and body posture in Drosophila. *Biological Cybernetics*.

Götz, K. and Wandel, U. (1984). Optomotor control of the force of flight in Drosophila and Musca. *Biological cybernetics*, pages 135–139.

Götz, K. G. (1968). Flight control in Drosophila by visual perception of motion. *Kybernetik*, 4(6):199–208.

Götz, K. G. (1975). The optomotor equilibrium of the Drosophila navigation system. *The Journal of Comparative Physiology*, 99:187–210.

Götz, K. G. (1987). Course-control, metabolism and wing interference during ultra-long tethered flight in Drosophila melanogaster. *Journal of Experimental Biology*, 128:35–46.

Graetzel, C. F., Nelson, B. J., and Fry, S. N. (2010). Frequency response of lift control in Drosophila. *Journal of the Royal Society, Interface / the Royal Society*, 7(52):1603–16.

Hardie, R. C. and Raghu, P. (2001). Visual transduction in Drosophila. *Nature*, 413(6852):186–193.

Hausen, K. (1993). Decoding of retinal image flow in insects. *Rev. Oculomot. Res.*, 5:203–235.

Hedrick, T. L., Cheng, B., and Deng, X. (2009). Wingbeat time and the scaling of passive rotational damping in flapping flight. *Science*, 324(5924):252–255.

Hedrick, T. L. and Robinson, A. K. (2010). Within-wingbeat damping: dynamics of continuous free-flight yaw turns in Manduca sexta. *Biology letters*, 6(3):422–5.

Heide, G. (1983). Neural mechanisms of flight control in Diptera. In Nachtigall, W., editor, *BioNaReport*, chapter Biona-Repo, pages 35–52. Fischer.

Heisenberg, M. and Wolf, R. (1984). *Vision in Drosophila. Genetics of Microbehaviour*. Springer, Berlin.

Heisenberg, M. and Wolf, R. (1988). Reafferent control of optomotor yaw torque in Drosophila melanogaster. *Journal of Comparative Physiology A*, 163(3):373–388.

Hengstenberg, R. (1988). Mechanosensory control of compensatory head roll during flight in the blowfly Calliphora erythrocephala Meig. *Journal of Comparative Physiology A*, 163:159–168.

Hengstenberg, R. (1991). Gaze control in the blowfly Calliphora: a multisensory two-stage integration process. *The Neurosciences*, 3:19–29.

Hesselberg, T. and Lehmann, F.-O. (2007). Turning behaviour depends on frictional damping in the fruit fly Drosophila. *The Journal of Experimental Biology*, 210(Pt 24):4319–4334.

Hollick, F. S. J. (1940). The flight of the dipterous fly Muscina stabulans Fallen. *Philosophical Transactions of the Royal Society B: Biological Sciences*, 230:383–392.

Humbert, J. S. and Faruque, I. a. (2011). Analysis of Insect-Inspired Wingstroke Kinematic Perturbations for Longitudinal Control. *Journal of Guidance, Control, and Dynamics*, 34(2):618–623.

Iriarte-Díaz, J. and Swartz, S. M. (2008). Kinematics of slow turn maneuvering in the fruit bat Cynopterus brachyotis. *The Journal of Experimental Biology*, 211(Pt 21):3478–89.

Jones, E., Oliphant, T., and Peterson, P. (2010). SciPy: Open source scientific tools for Python.

Josephson, R. K., Malamud, J. G., and Stokes, D. R. (2000). Asynchronous muscle : a primer. *Journal of Experimental Biology*, 203:2713–2722.

Khalil, H. K. (1996). *Nonlinear Systems*. Prentice-Hall, Inc., Upper Saddle River, 2nd edition.

Krapp, H. G. (2000). Neuronal matched filters for optic flow processing in flying insects. *Int. Rev. Neurobiol.*, 44:93–120.

Krapp, H. G. (2009). Ocelli. *Current Biology*, 19:435–437.

Krapp, H. G., Hengstenberg, B., and Hengstenberg, R. (1998). Dendritic structure and receptive-field organization of optic flow processing interneurons in the fly. *Journal of neurophysiology*, 79(4):1902–17.

Land, M. F. and Collett, T. S. (1974). Chasing behaviour of houseflies (Fannia canicularis). *Journal Of Comparative Physiology*, 89(4):331–357.

Lehmann, F.-O. and Dickinson, M. H. (1997). The changes in power requirements and muscle efficiency during elevated force production in the fruit fly Drosophila melanogaster. *The Journal of Experimental Biology*, 200(Pt 7):1133–43.

Lentink, D. and Dickinson, M. H. (2009). Rotational accelerations stabilize leading edge vortices on revolving fly wings. *Journal of Experimental Biology*, 212:2705–2719.

Maxworthy, T. (1979). Experiments on the Weis-Fogh mechanism of lift generation by insects in hovering flight. Part 1. Dynamics of the 'fling'. *Journal of Fluid Mechanics*, 93(01):47–63.

Maxworthy, T. (1981). The Fluid Dynamics of Insect Flight. *Ann. Rev. Fluid Mech.*, 13:329–350.

Medici, V. and Fry, S. N. (2012). Embodied linearity of speed control in Drosophila melanogaster. *Journal of the Royal Society, Interface / the Royal Society*, 9(77):3260–7.

Mielke, A. and Heide, G. (1993). Effects of artificially generated haltere nerve afferences on the activation of the flight steering muscles in Calliphora. In Elsner, N. and Heisenberg, M., editors, *Proceedings of the 21st Gottingen Neurobiology Conference*, page 207, Thieme, Stuttgart.

Murray, R. M., Li, Z., and Sastry, S. (1994). *A mathematical introduction to robotic manipulation*. CRC Press, New York.

Nalbach, G. and Hengstenberg, R. (1994). The halteres of the blowfly Calliphora. II. Three-dimensional organization of compensatory reactions to real and simulated rotations. *Journal of Comparative Physiology A*, 175:695–708.

Parsons, M. M., Krapp, H. G., and Laughlin, S. B. (2006). A motion-sensitive neuron responds to signals from the two visual systems of the blowfly, the compound eyes and ocelli. *Journal of Experimental Biology*, 209:4464–4474.

Parsons, M. M., Krapp, H. G., and Laughlin, S. B. (2010). Sensor fusion in identified visual interneurons. *Current biology : CB*, 20(7):624–8.

Pringle, J. W. S. (1948). The Gyroscopic Mechanism of the Halteres of Diptera. *Philosophical transactions of the Royal Society of London. Series B, Biological sciences*, 233(602):347–384.

Ramamurti, R. and Sandberg, W. C. (2007). A computational investigation of the three-dimensional unsteady aerodynamics of Drosophila hovering and maneuvering. *The Journal of Experimental Biology*, 210(Pt 5):881–96.

Ristroph, L., Bergou, A. J., Guckenheimer, J., Wang, Z. J., and Cohen, I. (2011). Paddling Mode of Forward Flight in Insects. *Physical Review Letters*, 106(17):1–4.

Ristroph, L., Bergou, A. J., Ristroph, G., Coumes, K., Berman, G. J., Guckenheimer, J., Wang, Z. J., and Cohen, I. (2010). Discovering the flight autostabilizer of fruit flies by inducing aerial stumbles. *Proceedings of the National Academy of Sciences of the United States of America*, 107(11):4820–4.

Ristroph, L., Berman, G. J., Bergou, A. J., Wang, Z. J., and Cohen, I. (2009). Automated hull reconstruction motion tracking (HRMT) applied to sideways maneuvers of free-flying insects. *The Journal of Experimental Biology*, 212(Pt 9):1324–1335.

Roth, E., Reiser, M., Dickinson, M. H., and Cowan, N. J. (2012). A Task-level Model for Optomotor Yaw Regulation in Drosophila Melanogaster: A Frequency-Domain System Identification Approach. In *Conference on Decisions and Controls*, Maui.

Sane, S. P. (2003). The aerodynamics of insect flight. *The Journal of Experimental Biology*, 206(23):4191–4208.

Sane, S. P. and Dickinson, M. H. (2001). The control of flight force by a flapping wing: lift and drag production. *The Journal of Experimental Biology*, 2626:2607–2626.

Sherman, A. and Dickinson, M. H. (2003). A comparison of visual and haltere-mediated equilibrium reflexes in the fruit fly Drosophila melanogaster. *The Journal of Experimental Biology*, 206(2):295–302.

Sherman, A. and Dickinson, M. H. (2004). Summation of visual and mechanosensory feedback in Drosophila flight control. *The Journal of Experimental Biology*, 207(1):133–142.

Shyy, W., Aono, H., Chimakurthi, S., Trizila, P., Kang, C.-K., Cesnik, C., and Liu, H. (2010). Recent progress in flapping wing aerodynamics and aeroelasticity. *Progress in Aerospace Sciences*, 46(7):284–327.

Strausfeld, N. J. (1984). Functional neuroanatomy of the blowfly's visual system. In Ali, M. A., editor, *Photoreception and Vision in Invertebrates*, pages 483–522. Plenum Press, New York.

Sugiura, H. and Dickinson, M. H. (2009). The generation of forces and moments during visual-evoked steering maneuvers in flying Drosophila. *PloS one*, 4(3):e4883.

Sun, M. and Wang, J. K. (2007). Flight stabilization control of a hovering model insect. *The Journal of Experimental Biology*, 210(Pt 15):2714–22.

Sun, M. and Xiong, Y. (2005). Dynamic flight stability of a hovering bumblebee. *The Journal of Experimental Biology*, 208(Pt 3):447–59.

Tammero, L. F. and Dickinson, M. H. (2002). The influence of visual landscape on the free flight behavior of the fruit fly Drosophila melanogaster. *The Journal of Experimental Biology*, 205(Pt 3):327–43.

Tammero, L. F., Frye, M. a., and Dickinson, M. H. (2004). Spatial organization of visuomotor reflexes in Drosophila. *The Journal of Experimental Biology*, 207(1):113–122.

Taylor, G. K. (2003). Dynamic flight stability in the desert locust Schistocerca gregaria. *The Journal of Experimental Biology*, 206(16):2803–2829.

Taylor, G. K., Bacic, M., Bomphrey, R. J., Carruthers, A. C., Gillies, J., Walker, S. M., and Thomas, A. L. R. (2008). New experimental approaches to the biology of flight control systems. *The Journal of Experimental Biology*, 211(Pt 2):258–66.

Taylor, G. K. and Krapp, H. G. (2008). Sensory Systems and Flight Stability: What do Insects Measure and Why. *Advances In Insect Physiology*, 34:231–316.

Taylor, G. K. and Zbikowski, R. (2005). Nonlinear time-periodic models of the longitudinal flight dynamics of desert locusts Schistocerca gregaria. *Journal of the Royal Society, Interface / the Royal Society*, 2(3):197–221.

Trimarchi, J. R. and Murphey, R. K. (1997). The shaking-B2 mutation disrupts electrical synapses in a flight circuit in adult Drosophila. *Journal of Neuroscience*, 17(12):4700–4710.

Tu, M. and Dickinson, M. H. (1994). Modulation of Negative Work Output From a Steering Muscle of the Blowfly Calliphora Vicina. *The Journal of Experimental Biology*, 192(1):207–24.

Tu, M. and Dickinson, M. H. (1996). The control of wing kinematics by two steering

muscles of the blowfly (Calliphora vicina). *Journal of Comparative Physiology A*, 178:813–830.

Van Breugel, F. and Dickinson, M. H. (2012). The visual control of landing and obstacle avoidance in the fruit fly Drosophila melanogaster. *Journal of Experimental Biology*, 215(11):1783–1798.

Vogel, S. (1966). Flight in Drosophila I. Flight performance of tethered flies. *The Journal of Experimental Biology*, 44:567–578.

Vogel, S. (1967). Flight in Drosophila. II. Variations in stroke parameters and wing contour. *The Journal of Experimental Biology*, 46:383–392.

Wang, H., Ando, N., and Kanzaki, R. (2008). Active control of free flight manoeuvres in a hawkmoth, Agrius convolvuli. *The Journal of Experimental Biology*, 211(Pt 3):423–32.

Williamson, W. R., Wang, D., Haberman, A. S., and Hiesinger, P. R. (2010). A dual function of V0-ATPase a1 provides an endolysosomal degradation mechanism in Drosophila melanogaster photoreceptors. *The Journal of Cell Biology*, 189(5):885–899.

Wisser, A. and Nachtigall, W. (1984). Functional-morphological investigations on the flight muscles and their insertion points in the blowfly Calliphora erythrocephala (Insecta, Diptera). *Zoomorphology*, 104(3):188–195.

Wu, J. H. and Sun, M. (2012). Floquet stability analysis of the longitudinal dynamics of two hovering model insects. *Journal of the Royal Society Interface*, 9(74):2033–46.

Xiong, Y. and Sun, M. (2007). Dynamic flight stability of a bumblebee in forward flight. *Acta Mechanica Sinica*, 24(1):25–36.

Zanker, J. M. (1988). On the mechanism of speed and altitude control in Drosophila melanogaster. *Physiological entomology*, 13:351–361.

Zanker, J. M. (1990). The Wing Beat of Drosophila Melanogaster. I. Kinematics. *Philosophical Transactions of the Royal Society B: Biological Sciences*, 327(1238):1–18.

Appendix A

Tensor product spline representation of stroke-averaged force and moment maps

The functions $f_n(\delta, s)$, $f_t(\delta, s)$, and $M(\delta, s)$, the aerodynamic force normal to the stroke plane, tangential to the stroke plane, and the aerodynamic pitch moment respectively as functions of the slip angle and velocity magnitude which were discussed in Chapter 3 were computed by fitting tensor product splines to the measured robotic fly data. These tensor product surfaces were plotted in pseudo-color in Figure 3.4. Here we report the spline coefficients that approximate these functions and their standard deviations which were derived through a bootstrapping procedure.

Consider two spline spaces:

$$\mathbb{S}_1 = \mathbb{S}_{d_1, \boldsymbol{\sigma}_1} = \mathrm{span}\left\{ \varphi_1, \ldots, \varphi_{n_1} \right\}, \tag{A.1}$$

$$\mathbb{S}_2 = \mathbb{S}_{d_2, \boldsymbol{\sigma}_2} = \mathrm{span}\left\{ \chi_1, \ldots, \chi_{n_2} \right\}, \tag{A.2}$$

where d is degree of the spline space, $\boldsymbol{\sigma}$ is the knot vector, and φ and χ are basis or B-splines. The tensor product surface is given by:

$$f(x, y) = \sum_{i=1}^{n_1} \sum_{j=1}^{n_2} c_{ij} \varphi_i(x) \chi_j(y), \tag{A.3}$$

or written more compactly as

$$f(x, y) = \boldsymbol{\varphi}(x)^T \boldsymbol{C} \boldsymbol{\chi}(y). \tag{A.4}$$

The coefficients for computing $f_n(\delta, s)$, $f_t(\delta, s)$, and $M(\delta, s)$ from Equation A.4 are given in Tables A.1-A.3 with $d_1 = d_2 = 3$ and the following knot vectors:

$$\boldsymbol{\sigma}_1 = \left(-\frac{\pi}{2}, -\frac{\pi}{2}, -\frac{\pi}{2}, -\frac{\pi}{2}, \frac{3\pi}{2}, \frac{3\pi}{2}, \frac{3\pi}{2}, \frac{3\pi}{2} \right), \tag{A.5}$$

$$\boldsymbol{\sigma}_2 = \left(0, 0, 0, 0, s_{max}, s_{max}, s_{max}, s_{max} \right), \qquad s_{max} = 6.6. \tag{A.6}$$

	C_{i1}	C_{i2}	C_{i3}	C_{i4}
C_{1j}	$-5.85 \times 10^2 \pm 1.4$	$-3.55 \times 10^2 \pm 3.9$	$-2.04 \times 10^2 \pm 4.0$	$9.88 \times 10^1 \pm 2.0$
C_{2j}	$-6.42 \times 10^2 \pm 2.9$	$-1.01 \times 10^3 \pm 9.0$	$-1.17 \times 10^3 \pm 9.9$	$-1.74 \times 10^3 \pm 4.9$
C_{3j}	$-5.59 \times 10^2 \pm 2.9$	$-4.60 \times 10^2 \pm 8.8$	$-1.38 \times 10^3 \pm 9.8$	$-1.39 \times 10^3 \pm 4.9$
C_{4j}	$-6.19 \times 10^2 \pm 1.4$	$-3.94 \times 10^2 \pm 3.7$	$-1.62 \times 10^2 \pm 3.8$	$6.56 \times 10^1 \pm 1.9$

Table A.1: Coefficients, $C_{ij} \pm \text{std}_{ij}$, used in computing $f_n(\delta, s)$ from Equation A.4

	C_{i1}	C_{i2}	C_{i3}	C_{i4}
C_{1j}	$9.05 \times 10^1 \pm 2.9$	$1.11 \times 10^2 \pm 6.3$	$1.17 \times 10^2 \pm 5.9$	$1.28 \times 10^2 \pm 2.5$
C_{2j}	$1.92 \times 10^1 \pm 6.1$	$-6.57 \times 10^2 \pm 15.2$	$-1.60 \times 10^3 \pm 15.3$	$-2.70 \times 10^3 \pm 7.0$
C_{3j}	$1.02 \times 10^2 \pm 6.1$	$9.19 \times 10^2 \pm 15.3$	$1.70 \times 10^3 \pm 15.9$	$3.02 \times 10^3 \pm 7.1$
C_{4j}	$5.07 \times 10^1 \pm 2.8$	$-6.86 \times 10^1 \pm 6.5$	$8.48 \times 10^1 \pm 6.0$	$-1.28 \times 10^2 \pm 2.5$

Table A.2: Coefficients, $C_{ij} \pm \text{std}_{ij}$, used in computing $f_t(\delta, s)$ from Equation A.4

	C_{i1}	C_{i2}	C_{i3}	C_{i4}
C_{1j}	$-2.24 \times 10^2 \pm 2.9$	$-2.23 \times 10^2 \pm 6.7$	$-2.31 \times 10^2 \pm 6.4$	$-2.55 \times 10^2 \pm 2.9$
C_{2j}	$9.52 \times 10^1 \pm 6.1$	$1.06 \times 10^3 \pm 15.7$	$2.20 \times 10^3 \pm 17.0$	$2.77 \times 10^3 \pm 8.0$
C_{3j}	$-3.27 \times 10^2 \pm 6.0$	$-1.37 \times 10^3 \pm 15.4$	$-2.33 \times 10^3 \pm 16.6$	$-2.98 \times 10^3 \pm 7.9$
C_{4j}	$5.20 \times 10^1 \pm 2.9$	$7.76 \times 10^1 \pm 6.6$	$-6.74 \times 10^1 \pm 6.4$	$4.69 \times 10^1 \pm 2.8$

Table A.3: Coefficients, $C_{ij} \pm \mathrm{std}_{ij}$, used in computing $M(\delta, s)$ from Equation A.4